Additive Manufacturing 52 (2022) 102618

Contents lists available at ScienceDirect

Additive Manufacturing

journal homepage: www.elsevier.com/locate/addma

Research paper

Synchronous involvement of topology and microstructure to design additively manufactured lattice structures

Behzad Bahrami Babamiri [a], Jason R. Mayeur [a], Kavan Hazeli [b,*]

[a] Mechanical and Aerospace Engineering Department, University of Alabama in Huntsville, USA
[b] Aerospace and Mechanical Engineering Department, The University of Arizona, USA

ARTICLE INFO

Keywords:
Lattice structure
Additive manufacturing
Optimization
Microstructure
Deformation mechanisms
FFT crystal plasticity

ABSTRACT

This article presents a methodical approach to optimize microstructure (e.g., the crystallographic texture) and topology (e.g., unit cell and struts) concurrently to improve the mechanical properties of additively manufactured metallic lattice structures (AMLS), i.e., yield strength and plastic flow stress. Full-field elasto-viscoplastic Fast Fourier Transform (EVP-FFT) crystal plasticity (CP) simulations are employed to determine the optimal microstructure. The CP model parameters were calibrated to measured macroscopic stress–strain response and microstructural data for polycrystalline samples of additively manufactured (AM) Inconel 718 with solution treated and aged (STA) microstructure. Since the crystallographic orientation of the constituent single-crystal grains with respect to the loading direction has a significant impact on the mechanical behavior of the material, stress projection factor analysis was used to determine four candidate textures to explore in for a given unit cell topology. Full-field crystal plasticity simulations were used to determine macroscale yield surface parameters for each of the considered textures, thereby enabling macroscale lattice unit cell simulations that account for the underlying microstructure. The calibrated microstructure-dependent yield surfaces are used to investigate the effect of different microstructures on the mechanical response of different LS topologies with the same relative density. The results show that in a texture with $< 111 >$ crystallographic direction, parallel to the loading direction, the tensile and compressive yield strength are 20% and 58% larger, respectively compared to the AM STA IN718 texture. Furthermore, when this texture is used in conjunction with the Rhoctan topology, the results demonstrate 50% improvement in both the yield strength and modulus of elasticity relative to previously optimized AMLS designs that did not directly account for microstructure. This simultaneous consideration of microstructure and topology during optimization, thus, significantly enhances the structural integrity of the AMLS.

1. Introduction

Lattice structures (LS) are three-dimensional (3D) structures composed of interconnected repeated unit cells made of struts and nodes. The key factors of the design space in an additively manufactured lattice structure (AMLS) could be decided between two hierarchical orders: (1) geometry and arrangement of the struts and unit cells (i.e., topology), and (2) the struts' microstructure. Fig. 1 shows how any changes in these factors give rise to different global mechanical behavior since the local resolved shear stress on one or more slip systems (the active slip systems) depends on the combined effect of topology and grains arrangement. If we have full control of the microstructure (e.g., grain orientation), a slight change in the strut's geometry and arrangement would yield a different property. For example, in Fig. 1a we are using the solution treated and aged (STA) Inconel 718 (IN718) microstructure (see [1]) as a constant variable then we alter the topology from Rhombic dodecahedron to Rhoctan at a 30% relative density. Details of the Rhoctan topology can be found in [1]. The effect of topology changes on mechanical behavior under quasi-static loading is shown in Fig. 1b. It is seen that the compressive yield strength increases by nearly 18% when the topology is changed from Rhombic dodecahedron to Rhoctan with the same microstructure. Similarly, the mechanical properties of a fixed topology (Fig. 1c) could be altered by changing grain orientation synthetically (see Section 5). For instance, the same grains shown in Fig. 1c could lead to 52% higher compressive yield strength if their Euler angles are aligned along $(0, 55°, 45°)$ relative to the loading direction (i.e., $\langle 111\rangle$ is parallel to the loading direction) in the same exact topology configuration. In general, the deformation mechanisms of polycrystalline materials in any form (e.g., fully dense solid or lattice structure) are governed by the

---

* Corresponding author.
E-mail address: hazeli@arizona.edu (K. Hazeli).

https://doi.org/10.1016/j.addma.2022.102618
Received 19 October 2021; Received in revised form 22 December 2021; Accepted 9 January 2022
Available online 12 February 2022

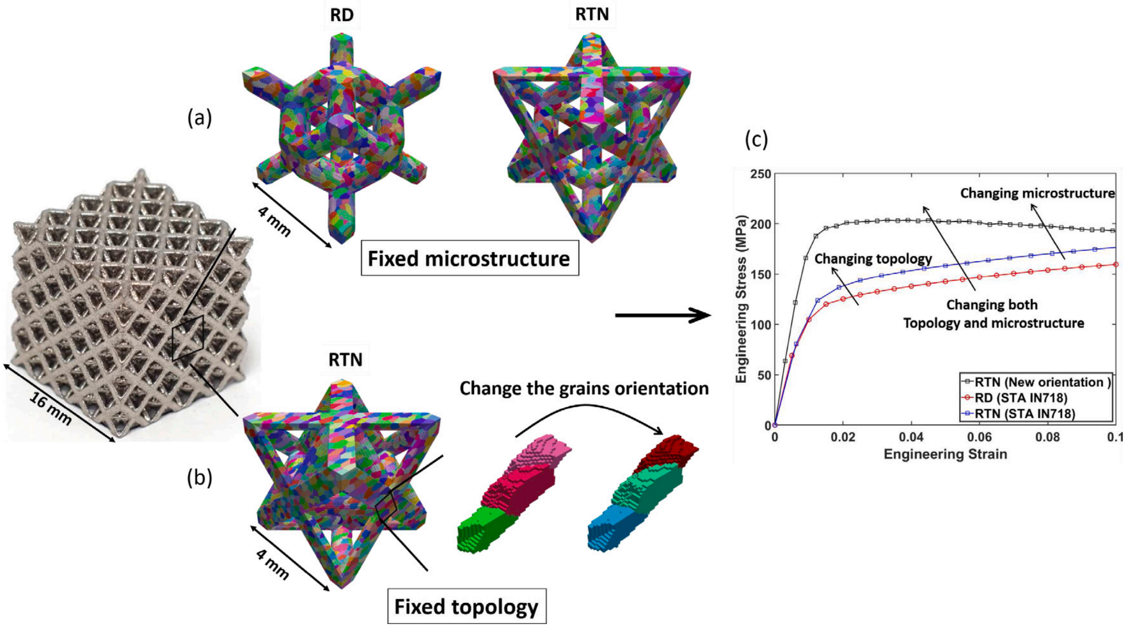

Fig. 1. Topology and microstructure are two main design variables in the additively manufactured lattice structure. The figure shows the effect of different topology and microstructure (i.e., different grain orientation) on the quasi-static compression response of STA IN718-AMLS. (a) When the microstructure and the relative density ($\rho^* = 30\%$) are fixed and the topology changes from Rhombic dodecahedron to Rhoctan, (b) when the topology is fixed at Rhoctan, and the microstructure is modified by aligning the grains along $(0, 55°, 45°)$ relative to the loading direction, and (c) shows the mechanical response of AMLS for both (a) and (b) cases.

dynamics and structure of microscopic features including interstitials and vacancies, voids, grain boundaries, orientation, and dislocations. In particular, the grain size, morphology, and orientation of the constituent single-crystal grains readily govern the mechanical properties and plastic deformation. Therefore, topology optimization [1–15] alone may not allow reaching AMLS full mechanical performance potential if the microstructural effects are not considered when designing them. It is worth mentioning that the optimization community never integrated the microstructure because it is too difficult to achieve this in the context of current mathematical programming formulations. The geometrical imperfections such as non-uniform struts, cross-sectional node area, and surface roughness due to manufacturing could also affect the mechanical behavior of AMLS. However, this study does not consider the effect of this geometrical imperfection. Note that the effect of struts diameter variation and the effect of porosity on the mechanical properties of AMLS made of IN718 are addressed in our previous studies, [16,17] there is still a need to investigate the manufacturing perspective of AMLS focusing on how to reduce the geometrical imperfection during the manufacturing process and how to account their influence in an optimized design.

Mechanical properties of AM parts could be controlled during the manufacturing process more readily than traditional manufacturing processes. This enables an additional level of design flexibility by spatially controlling the microstructural evolution. In other words, AM presents an opportunity where it is possible to derive the desired mechanical performance by influencing the microstructure during the build process [18]. In this regard, Plotkowski et al. [19], presented a new stochastic scan path generation algorithm in electron beam powder bed fusion (EB-PBF) AM that manipulates the spatial distribution of solidification conditions to control and optimize the grain structure in IN718. In another study using EB-PBF process, Gotterbarm et al. [18] fabricated IN718 samples with customized grain structure by changing the scan speed and beam power, including a single crystal IN718 in order to achieve a specific mechanical property.

The given examples highlight the remarkable potential of manufacturing complex topologies with desired microstructure using additive methods. In this article we are presenting a systematic integration of experiment and crystal plasticity, which serves as a design guideline, to find an optimized microstructure for a given topology to improve mechanical property performance compared to previously optimized topologies. It should be pointed out that we are not using the word optimized in the formal mathematical sense. We simply mean to imply that by considering both the effects of microstructure and topology, an improvement in the overall mechanical properties of an AMLS can be obtained. To determine the optimal microstructure for a given property objective, such as yield strength, a full-field Elasto-Viscoplastic Fast Fourier Transform (EVP-FFT) crystal plasticity (CP) model is used [20]. The parameters of the CP model were calibrated using the macroscopic experimental response of polycrystalline material as well as microstructural data obtained from AM STA IN718. Based on the stress projection factor analysis, four distinct microstructures with varying crystallographic textures are generated. Then, three different full-field virtual experiments, including uniaxial tension, compression, and shear, were performed on the generated microstructures using EVP-FFT to generate yield data for establishing microstructure-sensitive macroscopic yield surface parameters for the modified volumetric hardening model (MVHM). Finally, the calibrated MVHM is applied in finite element modeling to explore the influence of different microstructures on the mechanical response of various LS topologies with the same relative density.

2. Crystal plasticity-based framework

This section delineates the main components of a crystal plasticity framework including construction of 3D synthetic microstructures, description of the constitutive model, calibration of material parameters, and the post-processing procedure to generate the yield surface.

2.1. 3D Synthetic microstructure

Fig. 2 illustrates the process involved in the generation of 3D synthetic microstructure using 2D Electron Backscatter Diffraction (EBSD) scans. In AMLS, struts may take on various shapes and are often not parallel to the build direction. Due to the geometry-dependent nature of the solidification process, the development of microstructural

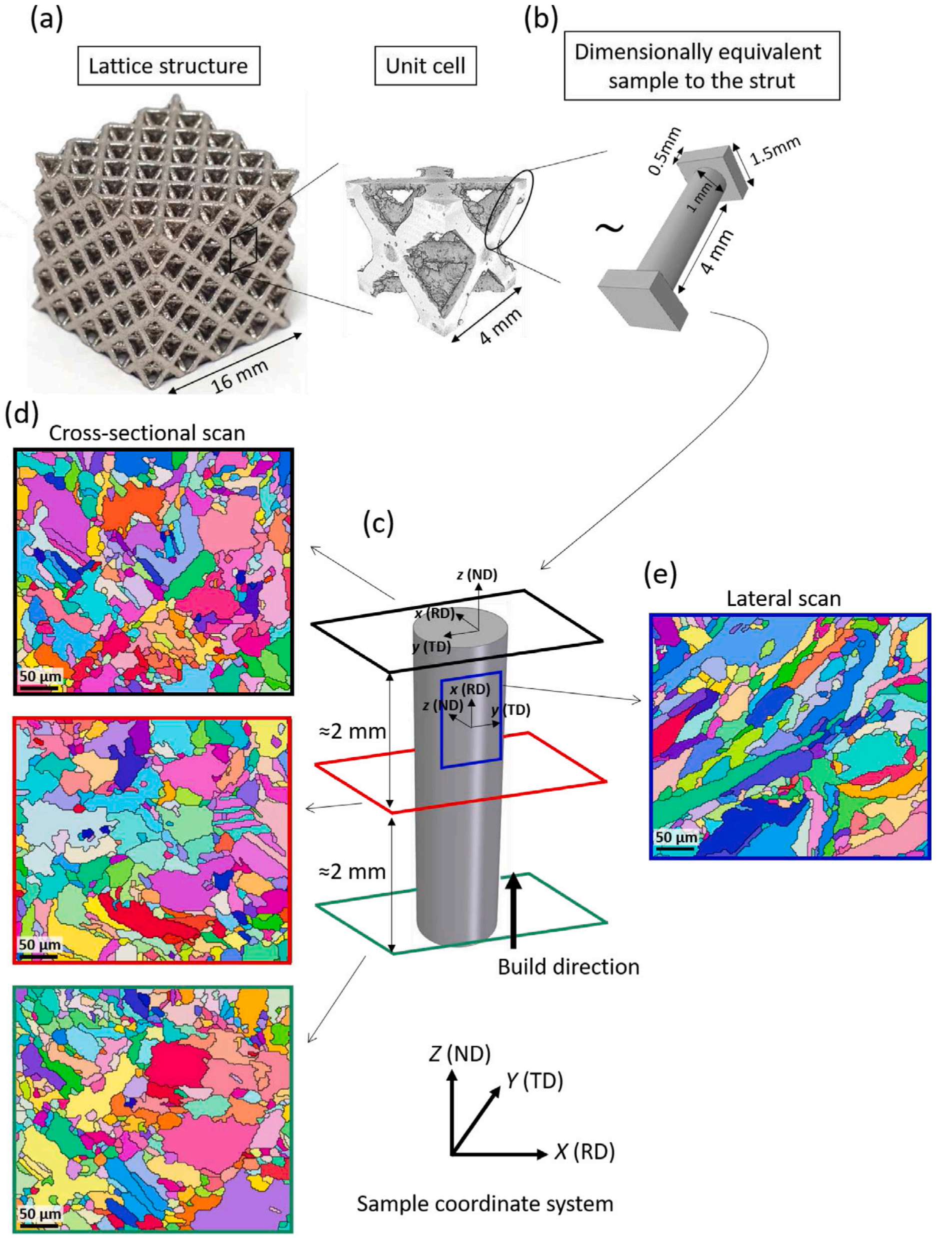

Fig. 2. The steps involved in the creation of the 3D synthetic polycrystalline microstructural instantiations starting from the EBSD data. (a) The AMLS made of IN718 with its unit cell and struts, (b) the AM sample manufactured with the same build direction and dimension as the strut in the AMLS, (c) the schematic of EBSD scan plane and direction to get initial crystallographic texture using the sample shown in b, (d) & (e) the 2D EBSD image of cross-sectional-area and the surface area of the sample, respectively.

characteristics such as grain size and orientation, porosity size and distribution, and surface roughness is also geometry-dependent. Therefore, the first step was to fabricate IN718 samples with the same dimension and build direction as the struts (see Fig. 2a & b). The material and laser parameters, as well as the scan strategy, that were used in the manufacturing of AM IN718 samples are detailed in [1]. To measure the initial crystallographic texture a strut was cut from the lattice structure, sectioned, mounted, and polished at three ≈ 2 mm spaced intervals along the build direction. At each interval we performed EBSD scans over the cross-sectional area of the strut. In addition, one scan was conducted along the lateral surface of the strut as shown in Fig. 2c. Locations of the EBSD scans and the corresponding texture are indicated in Fig. 2c, d, & e.

Relevant microstructural statistics are quantified, such as grain size and orientation distributions, are retrieved from the EBSD data in the first step using the reconstruction filters in DREAM.3D [36]. The reconstruction method includes the following steps: (a) removing experimental noise from the EBSD data, (b) transform data to reflect the same coordinate system on both map coordinates and Euler angles (either to Euler or spatial coordinate system), (c) segmenting grains using a misorientation threshold value, and (d) determining grain sizes and orientations. To reconstruct grains, it is essential to remove unreliable or non-indexed points from the map and replace them with (in general) more reliable orientations from neighboring pixels. When the cleaning procedure is complete, it is critical to transforming the data so that all the EBSD scans have the same coordinate system. This is important because there are two distinct scans with two different coordinate systems (i.e., cross-sectional and lateral area maps). Hence, first, the data transformed from a spatial coordinate system to the Euler angle reference frame for all four scans. This will keep the Euler angles while changing the map coordinates. Afterwards, the Euler angles for the cross-sectional scans were rotated −90° around z (ND), and for the lateral scans, the Euler angles were rotated 90° around z (ND) and x (RD), respectively. Fig. 3 shows the final EBSD orientation maps

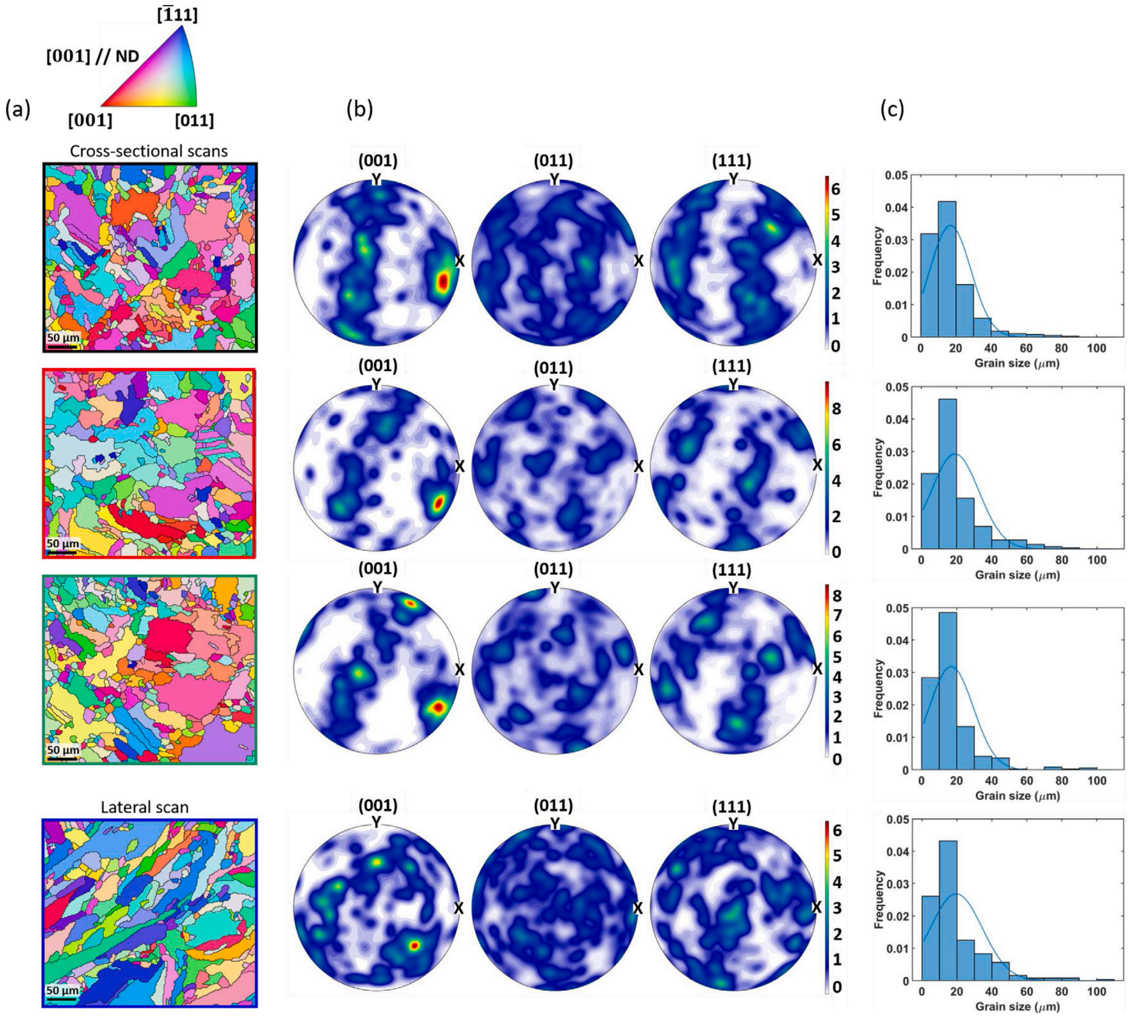

Fig. 3. EBSD maps and pole figures showing the initial microstructure and crystallographic texture in the samples of IN718: (a) 2D EBSD scan of cross-sectional and lateral area, (b) stereographic pole figures showing the initial crystallographic texture for each scan in AM IN718 sample, (c) the grain size distribution of each EBSD scan.

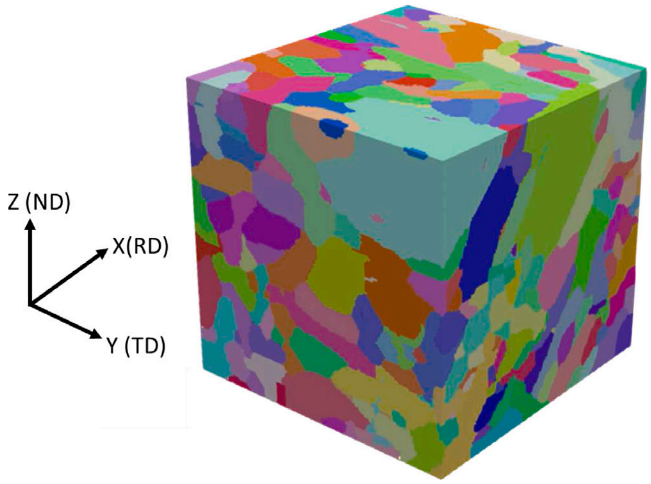

Fig. 4. 3D reconstruction of AM IN718 microstructure. The shown volume is the reconstruction of individual EBSD maps collected from cross-sectional and lateral area of the cylindrical sample (equivalent to the AMLS strut size) and has dimensions $64 \times 64 \times 64$ µm.

and pole figures, which reveal the initial microstructure and crystallographic texture, as well as the grain size distribution in the struts made of IN718. Additional information on these methods can be found in the DREAM.3D reconstruction tutorial and related algorithms [37].

In this study grain size is reported as the equivalent circle diameter, and the orientations follows Bunge Euler angles $(\varphi_1, \phi, \varphi_2)$ convention. Since the EBSD scans are 2D, stereological techniques are required to acquire the 3D grain sizes (diameter of the corresponding sphere) for an accurate microstructure representation. By multiplying a stereological factor of $4/\pi$ in 2D grain sizes, they will be converted to 3D grain size [37]:

$$\overline{R}_{3D} = \left(\frac{4}{\pi}\right)\overline{R}_{2D} \tag{1}$$

Next, 3D synthetic microstructures are created using the previously acquired statistics. DREAM.3D building filters are used for this purpose. The cross-sectional and lateral area's microstructure exhibit grains with average major axis $a = 13.3$ and 17 µm and minor axis $b = 6.8$ and 6.74 µm resulting in an aspect ratio of approximately 2 and 2.52, respectively. The average grain size in the material was approximately 18.15 µm. These parameters along with the crystallographic orientations from all of the EBSD scans are used as the inputs for generating the 3D statistically equivalent microstructures. Note that the creation of 3D microstructures is random in nature, i.e., when the DREAM.3D pipeline is run several times with the same set of inputs, different microstructure

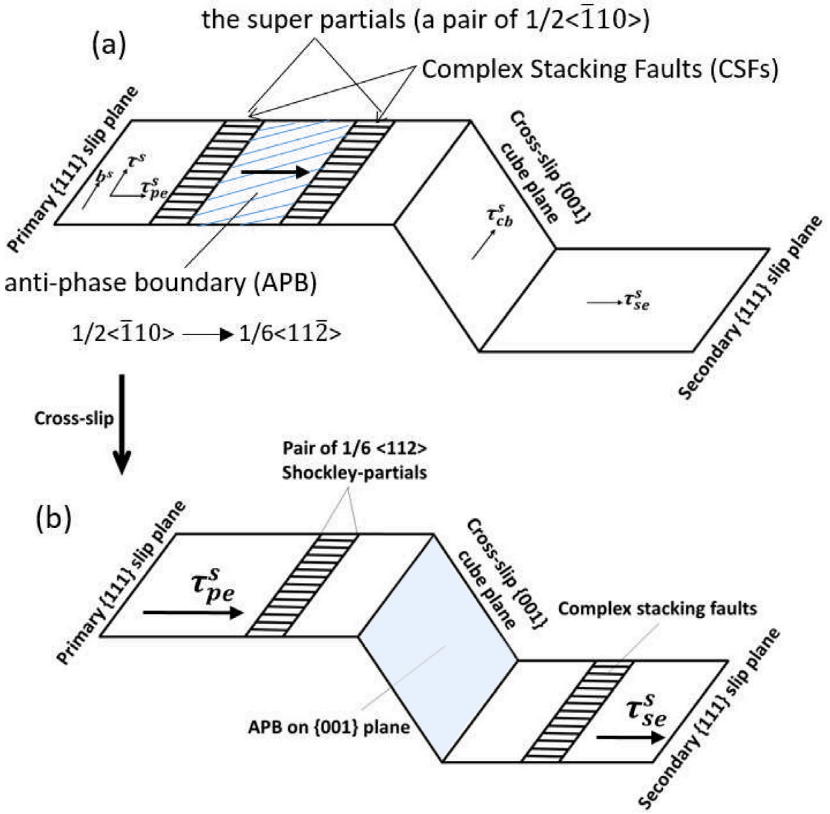

Fig. 5. The mechanisms of tension–compression asymmetry in an FCC structure due to formation of partials, cross-slip, and Kear Wilsdorf lock formation [21].

instantiations are produced. A representative 3D statistical equivalent microstructure is shown in Fig. 4. The 3D microstructure is a cube of 64 μm length. Approximately 800 to 1200 grains are present in the microstructure, which is adequate to represent the homogenized stress–strain behavior at the macroscale. The simulation input files for the EVP-FFT model are directly generated using a DREAM.3D filter. The rationale for using FFT is briefly discussed in Section 2.2. Several 3D microstructural instantiations are generated and used to investigate the effect of microstructure variability on the associated mechanical response.

2.2. Crystal plasticity fast fourier transform method (CP-FFT)

The FFT solution method for solving solid micromechanics problem was developed by [38] and initially applied to study the effective properties of linear elastic composite materials. It was subsequently extended to consider nonlinear elastic constitutive behavior for two-phase composites [39] and range of other increasingly complex constitutive behavior [40–43]. Lebensohn [44] was the first to use the approach in conjunction with full-field modeling of viscoplastic polycrystalline materials.

The FFT-based crystal plasticity methods are founded on the principle that the local mechanical response of a heterogeneous medium can be calculated as a convolution integral between Green function associated with appropriate fields of a linear reference homogeneous medium and the actual heterogeneity field. This method is appropriate for solving unit cell problems with periodic boundary conditions. Under these assumptions, the FFT solution is advantageous because it reduces the convolution integrals in *real space* to simple products in *Fourier space*. As a result, the heterogeneous field can be transformed into Fourier space using the FFT method. After that, the mechanical fields can be computed by the inverse FFT and returning to the original space. In addition to the periodic microstructure requirement, the FFT solver also requires the computational grid to be uniform and rectilinear. As such, the grid is not grain boundary conforming, and may lead to differences in local deformation and stress fields in the vicinity of grain boundaries relative to finite element simulation results that use grain boundary conforming meshes. For an in-depth examination of these issues the reader is referred to [45,46]. On the other hand, the FFT approach offers the advantages of not having to carry-out the time-consuming task of generating a grain boundary conforming mesh from a surface mesh and does not require the computationally expensive inversion of large matrices needed by the CP-FEM method [46], which results in a significant speed-up in simulation run-time for large polycrystalline microstructures.

Generally speaking, CP-FEM is the most common crystal plasticity formulation that has been applied to address full-field polycrystal plasticity problems. However, in CP-FEM, the input microstructure is often meshed with a large number of elements that conform to grain boundaries in order to provide a smoother solution to local field variations in the vicinity of the boundaries. Therefore, situations involving highly complex microstructures result in very large degree-of-freedom calculations that are computationally expensive and also susceptible to solution inaccuracy due to poor element shape. The simulation pre-processing step of generating a quality boundary conforming FEM mesh on a complex microstructure is itself quite time consuming and non-trivial. On the other hand, regular grids such as those used in CP-FFT do not suffer from these complications. Furthermore, crystal plasticity based on the FFT formulation is solved separately in each voxel, allowing the CP-FTT to be readily parallelized and adapted on supercomputers with many processors, which is an efficient method to reduce computational time. Thus, the CP-FFT formulation has received considerable attention because of its advantages such as lower computational time over CP-FEM mentioned above [40,44–48].

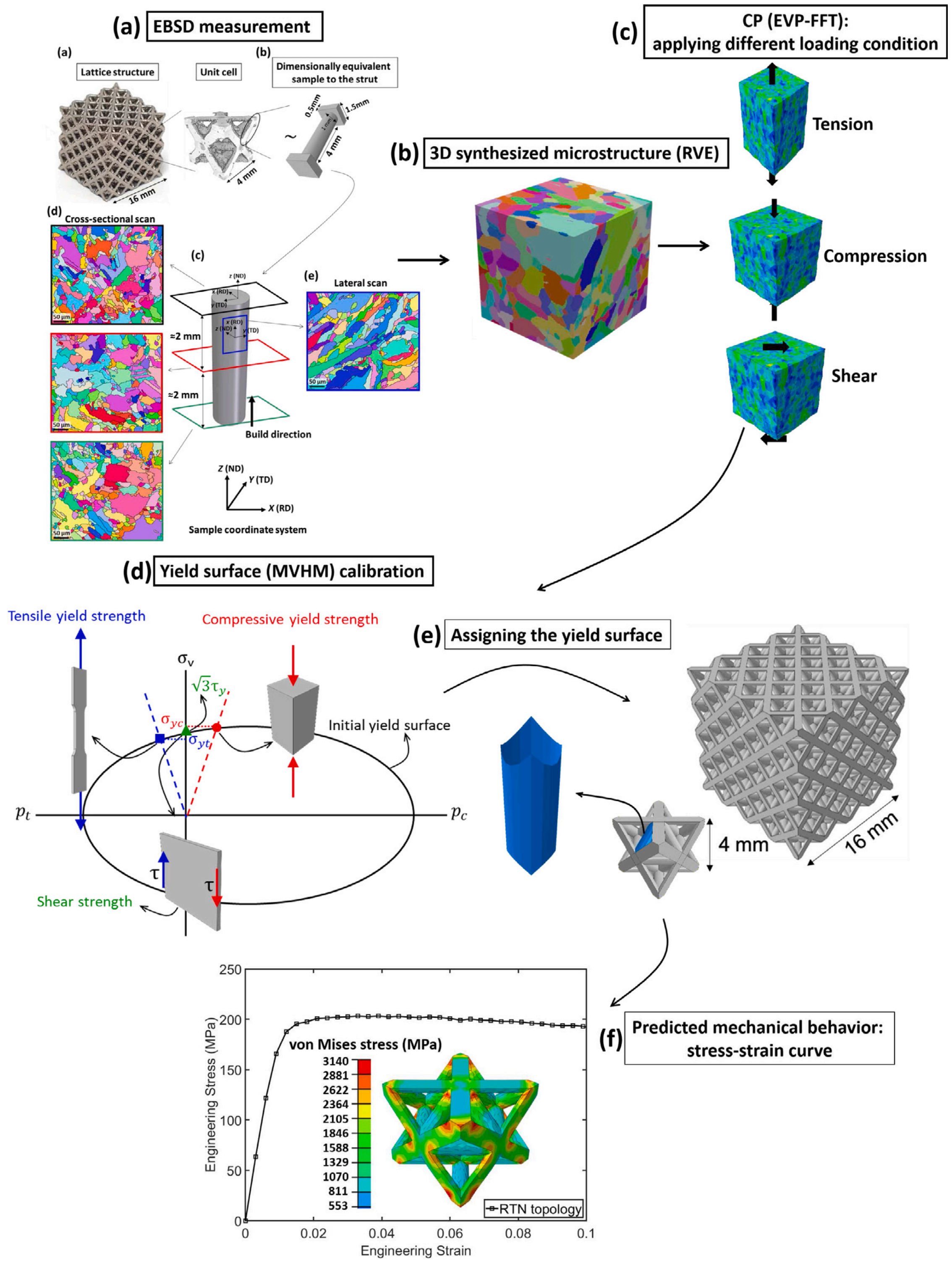

Fig. 6. The schematic of virtual lab to calibrate the MVHM for AM IN718, (a) the EBSD measurement of AM IN718 sample mimicking the dimension and the build direction of the LS strut, (b) generating 3D synthetic microstructure (RVE) from 2D EBSD maps, (c) using CP (EVP-FFT) modeling to apply different loading to the RVE in order to calibrate the MVHM yield surface, (d) calibration of MVHM by implementing the yield points, including tensile, compressive, and shear strength, from EVP-FFT simulation, (e) assigning the MVHM yield surface to the building struts to (f) predict the mechanical response of different LS topology.

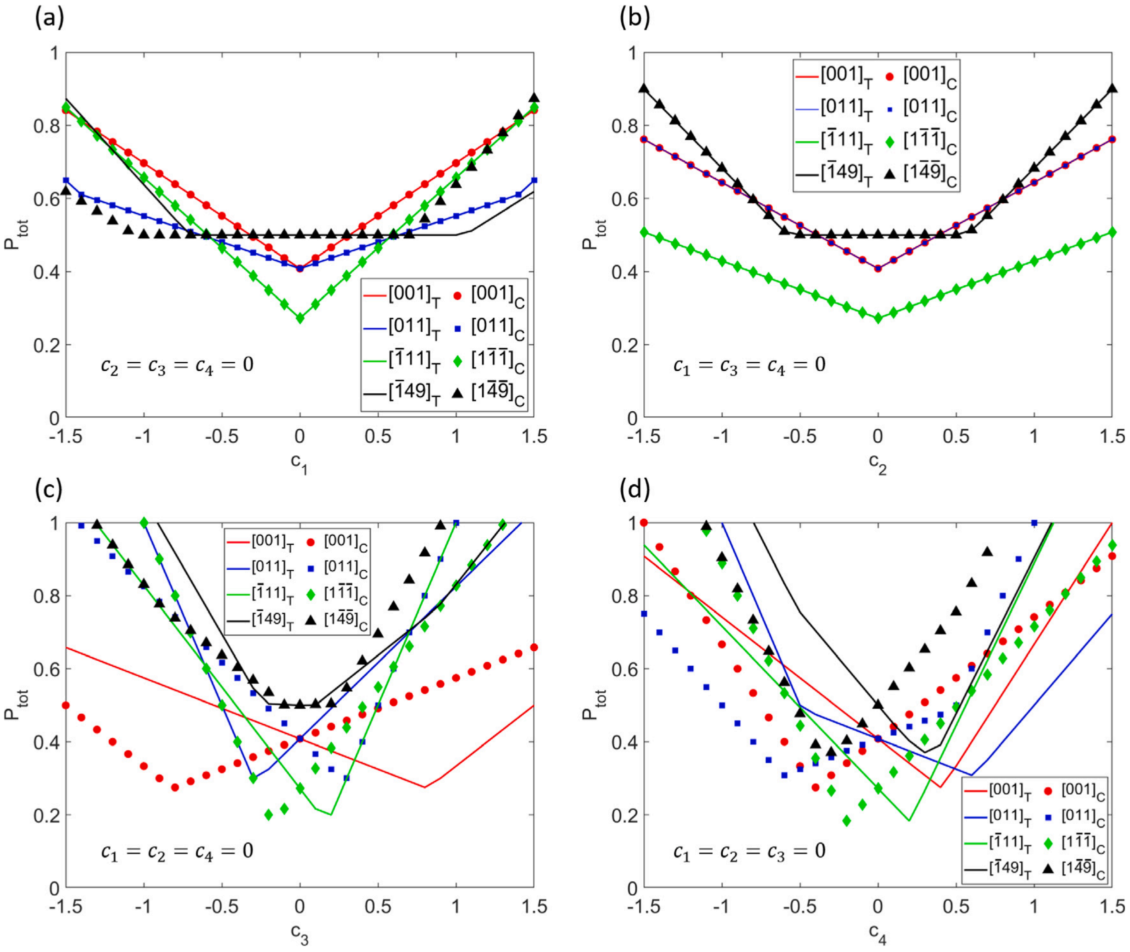

Fig. 7. Effects of non-Schmid constants on P_{tot} under uniaxial tension (T) and compression (C) for [001], [011], $[\bar{1}11]$, and $[\bar{1}49]$ loading axes.

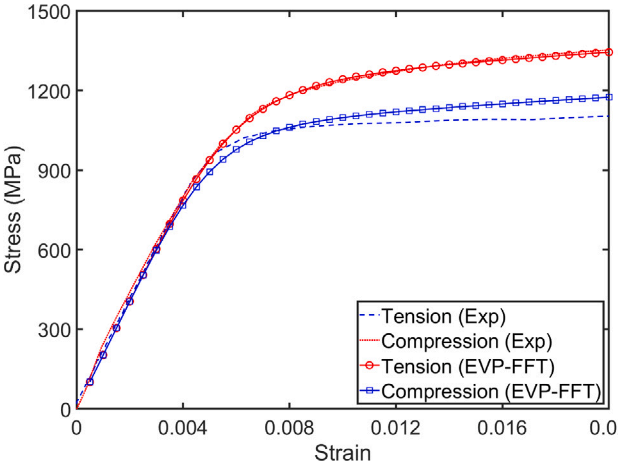

Fig. 8. The stress–strain curve from both experimental results [1] and simulation (EVP-FFT) for STA IN718.

2.2.1. Elastic viscoplastic formulation

In the full field EVP-FFT method, the SVE defined in Section 2.1 is divided into equally spaced voxels along the sample reference directions to represent the polycrystalline domain [20]. The elastic behavior is governed by anisotropic Hooke's law and the viscoplastic behavior is described using a power law relationship [20,44], i.e.

$$\sigma_{ij} = \mathbb{C}_{ijkl}\varepsilon^{e}_{kl} \tag{2}$$

$$\dot{\gamma}^s = \dot{\gamma}_0 \sum_{s=1}^{N} \left(\frac{\left| \boldsymbol{P}_{tot} : \boldsymbol{\sigma} \right|}{\tau^s_c} \right)^n sgn(\boldsymbol{P}^s_{sc} : \boldsymbol{\sigma}) \tag{3}$$

$$\dot{\varepsilon}^p_{ij} = \sum_{s=1}^{N} \boldsymbol{P}^s_{sc}\dot{\gamma}^s \tag{4}$$

$$\boldsymbol{P}^s_{ns} = c_1(\boldsymbol{t}^s \otimes \boldsymbol{b}^s) + c_2(\boldsymbol{t}^s \otimes \boldsymbol{n}^s) + c_3(\boldsymbol{n}^s \otimes \boldsymbol{n}^s) + c_4(\boldsymbol{t}^s \otimes \boldsymbol{t}^s) - (c_3 + c_4)(\boldsymbol{b}^s \otimes \boldsymbol{b}^s) \tag{5}$$

$$\boldsymbol{P}^s_{sc} = \frac{1}{2}(\boldsymbol{b}^s \otimes \boldsymbol{n}^s + \boldsymbol{n}^s \otimes \boldsymbol{b}^s) \tag{6}$$

$$\boldsymbol{P}_{tot} = \boldsymbol{P}^s_{sc} + \boldsymbol{P}^s_{ns} \tag{7}$$

Herein, tensor quantities $\mathbf{C}_{ijkl}$, ε^e_{kl}, and $\boldsymbol{P}_{tot}$ are elastic stiffness, elastic strain, and the total stress projection tensor. $\boldsymbol{P}^s_{sc}$ stands for the Schmid tensor, $\boldsymbol{P}^s_{ns}$ is the non-Schmid tensor, $\dot{\gamma}_0$ is the reference shear rate (taken here to be 0.001/s), n is the inverse of the material strain rate-sensitivity exponent (taken here to be 5), and τ^s_c represents the critical resolved shear stress (CRSS) on each slip system. In Eq. (4) N stands for the total number of active slip systems during plastic deformation.

Asymmetric plastic flow behavior of IN718 (i.e., tension-compression asymmetry behavior of IN718) is reported in several different investigations [16,17,21,49,50]. Therefore, IN718 does not obey the Schmid law, which has been attributed to the core structure of screw dislocations (formation of partials, cross-slip and lock formation). In our model, we accounted for the non-Schmid behavior effect by modifying the flow rule to incorporate additional stress projections Eq. (5) to capture the tension–compression asymmetry [51,52].

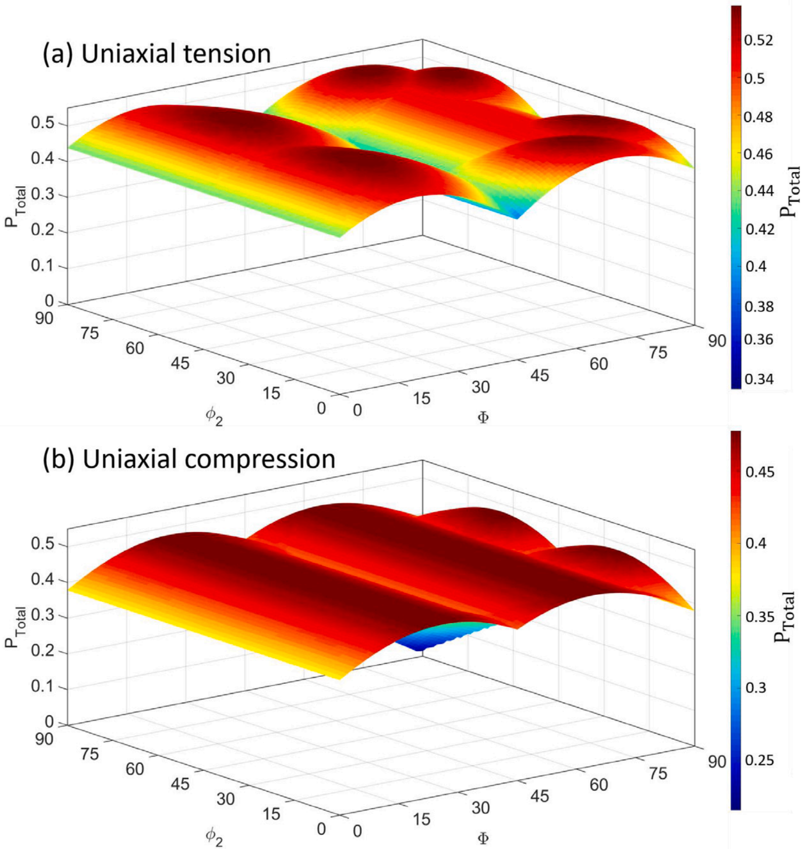

Fig. 9. The effect of ϕ_2 and Φ on the stress projection factor P^s_{tot} of a single crystal. (a) For tension, and (b) compression along Z direction.

The dislocation mechanisms responsible for the tension–compression asymmetry due to the non-Schmid effect is explained with the schematic presented in Fig. 5. As shown in Fig. 5a the super-dislocation, which is a pair of adjacent regular $1/2\langle\bar{1}10\rangle$ dislocations, gets dissociated into two super partials separated by an anti-phase boundary (APB) [53,54]. The APB energy on the $\{111\}$ plane is quite high, allowing for the slip of a single $1/2\langle\bar{1}10\rangle$ partial dislocation to occur. The high value APBs of separated $1/2\langle\bar{1}10\rangle$ partials makes them move in pairs [55]. These pairs of $1/2\langle\bar{1}10\rangle$ partials may also dissociate into $1/6\langle 11\bar{2}\rangle$ Shockley partials, that are separated by complex stacking faults (CSFs) (see Fig. 5a). The $\{001\}$ plane has a lower APB energy than the $\{111\}$ plane, which serves as a driving factor for super partials to cross-slip from the $\{111\}$ main octahedral slip plane onto the $\{001\}$ cube plane [56]. The extended dislocation core, on the other hand, is constrained to glide in the $\{111\}$ plane of its fault. While an extended screw dislocation cannot cross-slip, it may create a constriction and then travel freely to other planes, e.g., $\{001\}$ or $\{111\}$ [57]. Such dislocations may further cross-slip onto a secondary $\{111\}$ plane . The APB, on the other hand, is located on the $\{001\}$ plane, leading to the dislocation core being extended onto three planes: the main octahedral plane, the cube plane, and the secondary octahedral plane resulting in pinning of the dislocation segments. The shear stresses resolved on the main (p) and secondary (s) $\{111\}$ slip planes in the edge (e) direction, τ_{pe} and τ_{se}, induce the Shockley partials to constrict. Fig. 5b depicts these slip planes schematically. When tension or compression is applied in one direction, these resolved stresses constrict the Shockley partials, promoting cross-slip. When the direction of the applied stress is reversed, the Shockley partials are extended by τ_{pe} and τ_{se} which prevents cross-slip from occurring. As a result, the impact of the stresses is to increase the yield stress in one direction, while the effect of the stress in the other direction is to reduce it, resulting in the observed tension–compression asymmetry.

The geometry of a slip system, denoted by the symbol s, is defined by a unit vector aligned with the Burgers direction $\boldsymbol{b}^s$, and a unit vector aligned with the slip system plane normal, denoted by the symbols $\boldsymbol{n}^s$, and a unit vector perpendicular to the Burgers vector and normal directions $\boldsymbol{t}^s = \boldsymbol{b}^s \times \boldsymbol{n}^s$. IN718 has an FCC crystal structure and we employ 24 crystallographic $\{111\}\langle 110\rangle$ slip systems (considering forward and backward directions independently due to non-Schmid effect) i.e., 12 positive ($s+$) and 12 negative ($s-$) directions. The non-Schmid coefficients c_1, c_2, c_3, c_4, ideally should be determined using a single crystal experiment, however, since such data is currently unavailable they are determined by calibrating to monotonic tension–compression stress–strain data for a polycrystalline material. It is noted that c_1 and c_2 have a minor impact on tension–compression asymmetry, while the c_3 and c_4 play a significant role. This will be discussed in upcoming sections.

2.2.2. Hardening law

The evolution of the CRSS is described using the Generalized Voce Hardening Law [58]:

$$\tau_c^s(\Gamma) = \tau_0^s + (\tau_1^s + \theta_1^s\Gamma)\left[1 - exp\left(-\left|\frac{\theta_0^s}{\tau_1^s}\right|\Gamma\right)\right] \tag{8}$$

$$\Gamma = \int_0^t \sum_{s=1}^{N} |\dot{\gamma}|\, dt \tag{9}$$

where τ_0^s and θ_0^s are the initial shear stress and hardening rate, respectively. τ_1^s and θ_1^s are the saturation stress and hardening rate, respectively. τ_1^s and θ_1^s describe the asymptotic behavior of the material. The following expression is used to account for latent hardening effects as a result of the interactions between slip systems

$$\dot{\tau}_c^s = \frac{d\tau_c^s}{d\Gamma} \sum_{s'=1}^{N} h^{ss'} |\dot{\gamma}^{s'}| \tag{10}$$

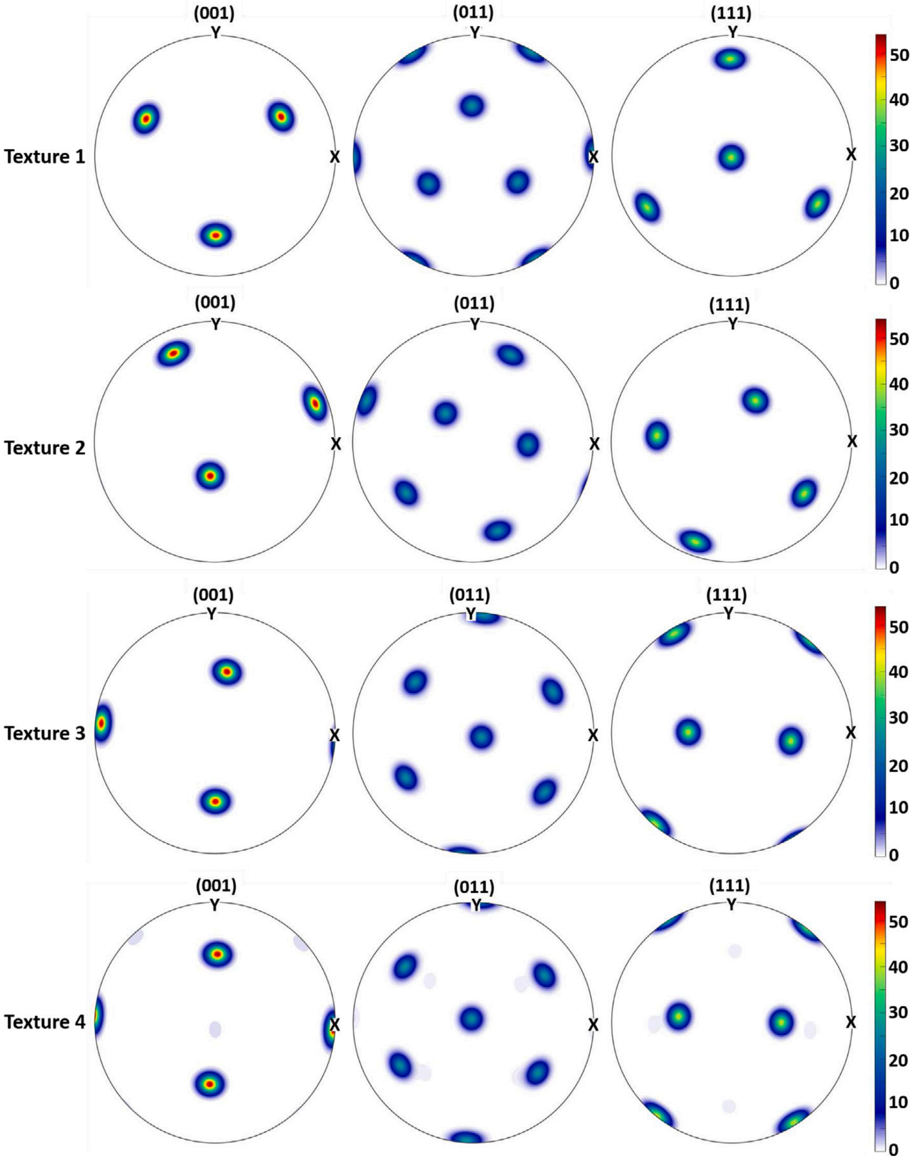

Fig. 10. The pole figure representation of different crystallographic orientation for four generated grain orientation texture based on the stress projection factor P_{tot}^{s}.

Here $\frac{d\tau_c^s}{d\Gamma}$ is self-hardening modulus and $h^{ss'}$ is the slip system interaction matrix.

3. Scale transition from microstructure-scale simulations to parameterization of the macroscale yield function

The goal of the approach described here is to provide stress–strain data obtained from the mesoscale simulations to identify macroscale yield surface parameters for the modified volumetric hardening model (MVHM) that accounts for the material's microstructure. Here, the microstructure is meant to include the grain size, orientation, morphology, and crystallographic texture. In this study, the MVHM yield surface is used, since in the case of AMLS, when the yield surface is assigned to the respective struts, it can capture the softening and hardening of the flow stress response during deformation, and it also accounts for (1) strut-level tension–compression asymmetry; (2) aggregate tension–compression asymmetry; and (3) strut-level hydrostatic pressure sensitivity [1,16].

3.1. The volumetric hardening model

The yield surface for MVHM is defined in terms of hydrostatic pressure (p) and von Mises stress σ_V i.e., $F(p, \sigma_V)$:

$$F(p, \sigma_V) = \sqrt{\sigma_V^2 + \alpha^2 (p - p_0)^2} - B = 0 \tag{11}$$

where

$$\alpha = \frac{3\sigma_c}{\sqrt{(3p_t + \sigma_c)(3p_c - \sigma_c)}}, \quad p_0 = \frac{p_c - p_t}{2}, \quad B = \alpha\left(\frac{p_c + p_t}{2}\right)$$

$$\sigma_V = \sqrt{\frac{3}{2}\sigma_{dev} : \sigma_{dev}} \tag{12}$$

$$p = -\frac{1}{3}\, trace\, \sigma \tag{13}$$

Here, σ_c is the yield strength under uniaxial compression, and p_c and p_t are yield strength in hydrostatic compression and yield strength in hydrostatic tension, respectively.

According to Eq. (11), the yield function contains three parameters that need to be determined: p_c, p_t, and σ_c. As a result, at least three unique points or three different loading paths are needed to construct

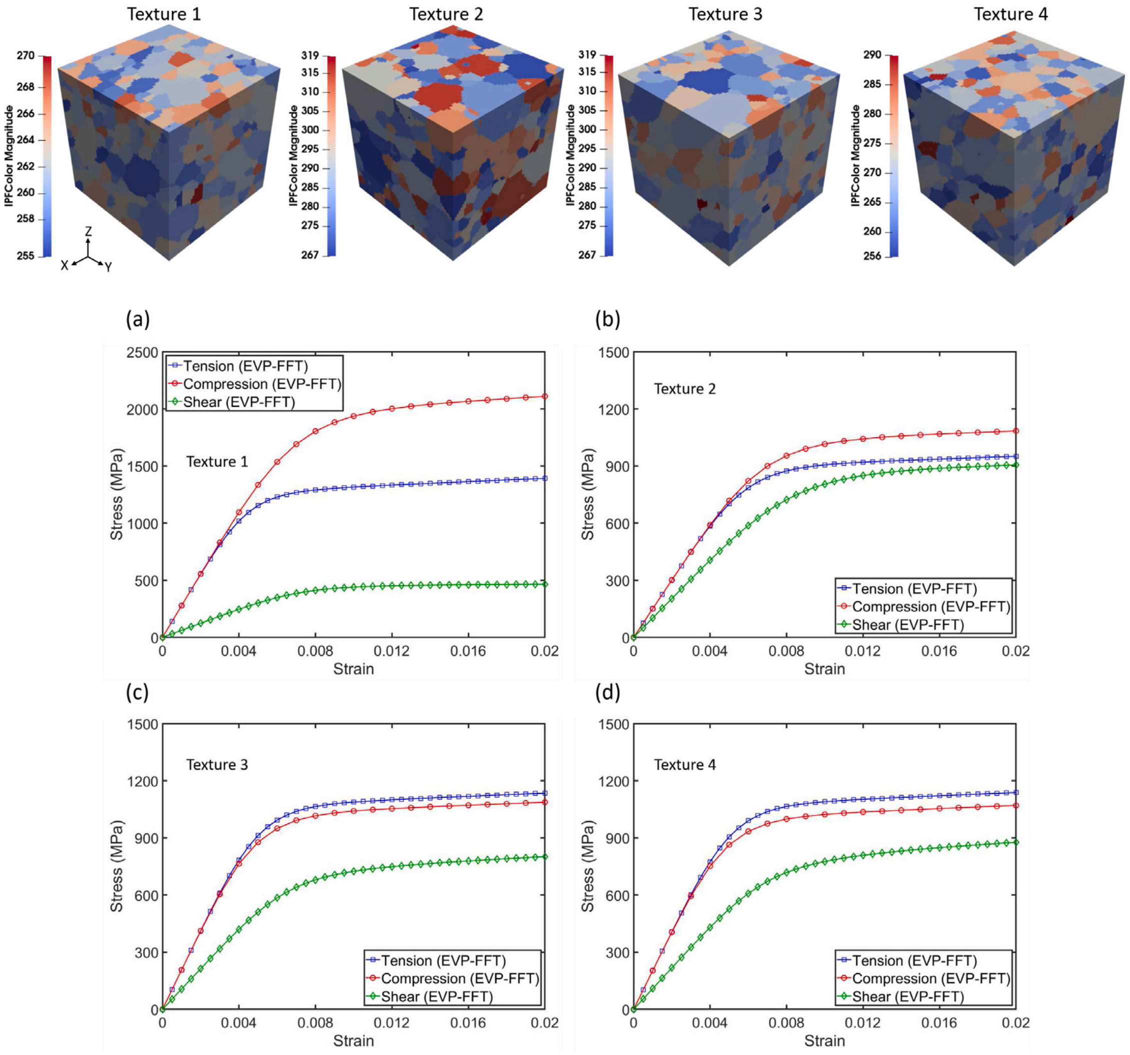

Fig. 11. The stress–strain response of all generated crystallographic orientation texture cases under uniaxial tension, compression and shear loading, (a) Texture 1: P^s_{tot} is minimum, (b) Texture 2: P^s_{tot} is maximum, (c) Texture 3: $P^T_{tot} = P^C_{tot}$, and (d) Texture 4: maximum value of $P^C_{tot} - P^T_{tot} > 0$.

the yield surface [1,16]. In the present work, yield strengths in tension, compression, and shear are selected as three distinct points from which to parameterize the initial yield surface. This data will be obtained from calibrated CP-FFT simulations. This approach enables the exploration of microstructure–property relationships virtually during the design/optimization process without the need to print and test parts, which is costly and time consuming, during this iterative process.

The CP model can accurately describe the anisotropic behavior of polycrystalline materials and naturally incorporate stress and strain partitioning across various phases, grains, and subgrains since it accounts for crystallographic texture and intrinsic single-crystalline anisotropy [59]. A significant impediment to the use of CP models for engineering simulations of large-scale components such as AMLS is it is computationally expensive. At the engineering scale, analytical yield functions such as MVHM are utilized instead of full-field CP simulations to predict and characterize the mechanical behavior of AMLS due to their computational efficiency and straightforward implementation. Fig. 6 depicts a conceptual representation of our approach to virtual experiments, which employ the CP-FFT method [20] and MVHM formulation.

When the constitutive parameters used in the current CP model are calibrated using the macroscopic experimental response of a polycrystalline material (see Section 4.1c), the virtual laboratory tool was employed to generate the yield stress points to determine the MVHM yield function parameters (see Fig. 6d). To uniquely determine the yield surface parameters including p_c, p_t, and σ_c, at least three distinct load paths must be considered. A nonlinear least square technique (NLSM) employing the Levenberg–Marquardt NLSM optimization algorithm is used to determine the best fitting parameter set [60,61]. The hardening behavior was calculated using uniaxial compression yield stress against logarithmic plastic strain. Uniaxial compression simulations were carried out up to 10% strain in order to get the uniaxial compression flow stress curve. The nominal stresses and strains were converted to true stresses and logarithmic plastic strains, which were then utilized as input data in Eq. (14). Note that an assumption of the the MVHM is that hardening only occurs under compressive hydrostatic loading ($p_t = const.$).

$$p_c = \frac{\sigma_c(\epsilon^{pl}_{axial})[\sigma_c(\epsilon^{pl}_{axial})(\frac{1}{\alpha^2}+\frac{1}{9})+\frac{p_t}{3}]}{p_t+\frac{\sigma_c(\epsilon^{pl}_{axial})}{3}} \tag{14}$$

4. Experiment-based model generation

4.1. Material characterization

Polycrystalline simulations using the microstructures discussed in 2.1 are used to calibrate the EVP-FFT model for bulk IN718 against the corresponding experimental measurements [1]. The material exhibits

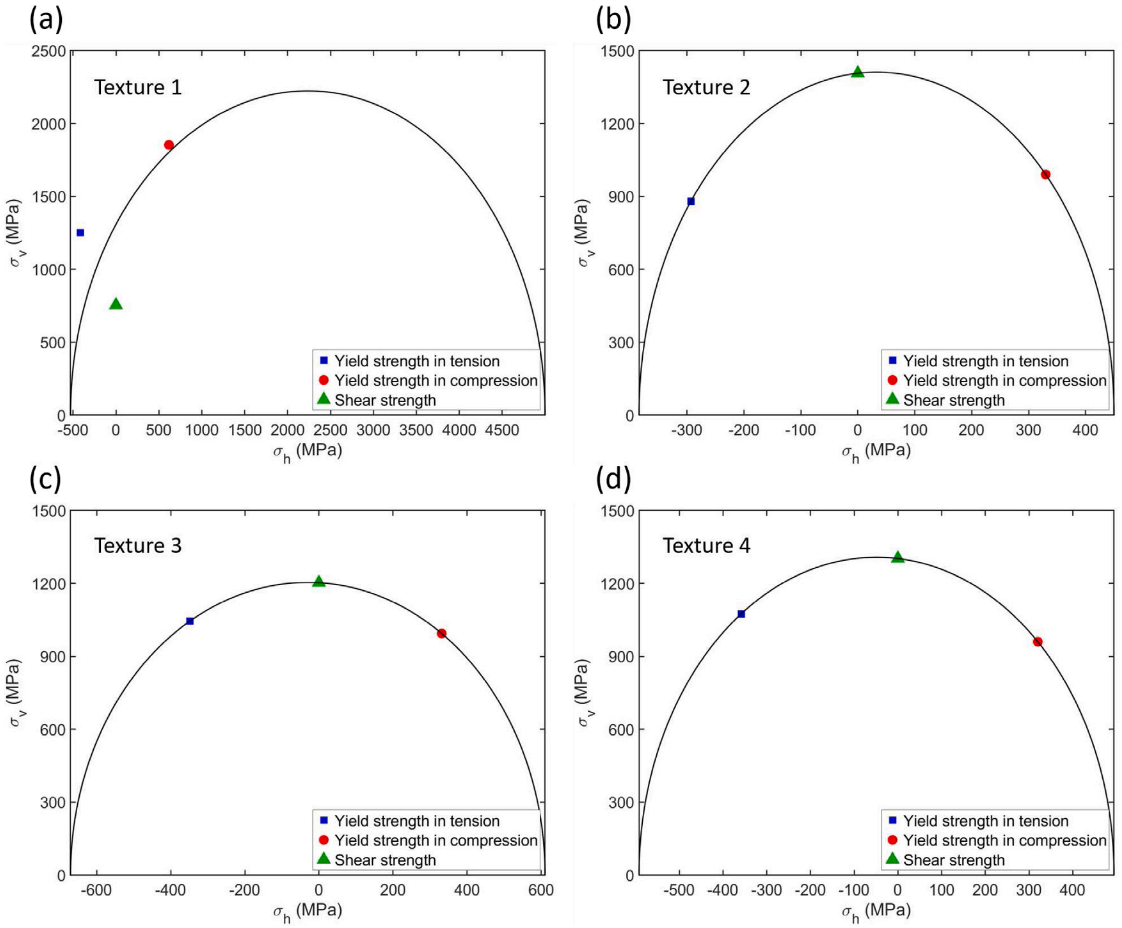

Fig. 12. MVHM yield surfaces of four different textures predicted by the EVP-FFT model.

mild anisotropy and tension–compression asymmetry. Thus, the constitutive parameters such as the Voce law hardening and non-Schmid parameters are calibrated in accordance with best fit between the experimental [1] and the simulation data.

The impact of non-Schmid constants on $\mathbf{P}_{\mathbf{tot}}$ is demonstrated in Fig. 7 for uniaxial tension and compression along the [001], [011], [$\bar{1}$11], and [$\bar{1}$49] axes. The stress projection factor, a generalization of the notion of Schmid factor to the non-Schmid case, for a slip system α is calculated from $P^{\alpha}_{tot} = \nu \cdot \mathbf{P}^{\alpha}_{\mathbf{tot}} \nu$ for a loading axis aligned along $\boldsymbol{\nu}$ (see Eqs. (5), (6), and (7)). Each non-Schmid constant was varied between −1.5 and 1.5, while all other non-Schmid constants were set to zero. Depending on the direction and sign of the loading axis, each shear stress component has a distinct impact on yield. It should be pointed out that the effects of c_2 on $\boldsymbol{P}_{tot}$ for tension and compression are similar, indicating that $\tau_{tn} = \mathbf{t} \cdot \boldsymbol{\sigma}\mathbf{b}$ does not contribute to the tension–compression asymmetry (see Fig. 7b). Similarly, c_2 does not contribute to the tension–compression asymmetry of all loading axis except [$\bar{1}$49] when $|c_1|$ is higher than 0.5. From Fig. 7a, it is observed that c_1 has the same impact on [001] tension and [001] compression as it does on [001] tension and [011] compression. Additionally, for the [001] loading axis, c_1 and c_2 have the same impact on $\boldsymbol{P}_{tot}$ under tension and compression. On the other hand, Fig. 7c & d indicate that c_3 and c_4 play the major role in capturing the tension–compression asymmetry for this particualr non-Schmid formulation. As a result, in this work, only c_3 and c_4 coefficients were used to capture the non-Schmid behavior. Tables 1 & 2 contain a list of the material parameters that were used for EVP-FFT simulations and Fig. 8 compares the computed stress–strain curves with the experimental results. Using the same calibrated parameters listed in Table 1, stress–strain curves for the three additional deformation modes (tension, compression, and shear) were created and simulated for the generated textures (see Section 5).

Table 1
Material parameters of IN718 alloy according to the experimental data of Babamiri et al. [1].

C_{11} (MPa)	C_{12} (MPa)	C_{44} (MPa)	τ_0 (MPa)	τ_1 (MPa)	θ_0 (MPa)	θ_1 (MPa)	n	$\dot{\gamma}_0$ (1/s)
259.6	179	109.6	470.5	166.5	900	40	5	10^{-3}

Table 2
Non-Schmid constants.

c_1	c_2	c_3	c_4
0	0	−0.06	−0.06

4.2. Synthetic orientation texture generation

To investigate the effect of grain orientation on the mechanical properties of the polycrystalline material, such as yield strength and elastic modulus, four different crystallographic textures are created with respect to the loading direction. The goal is finding the optimized distribution of the crystallographic orientation of the constituent single-crystal grains in the polycrystalline structure to improve the mechanical properties of AMLS.

Considering a uniaxial tension or compression along an arbitrary crystal axis, The slip system with the highest Schmid factor is activated in the case of associative flow, which is also known as the baseline case. As a result, the minimal inverse Schmid factor, also known as the orientation factor, is a helpful measure to determine the intensity of the coupling between applied stress and primary slip. However, the Schmid factor does not define the most favorable slip systems for a given applied stress in the case of non-associative flow. Rather the

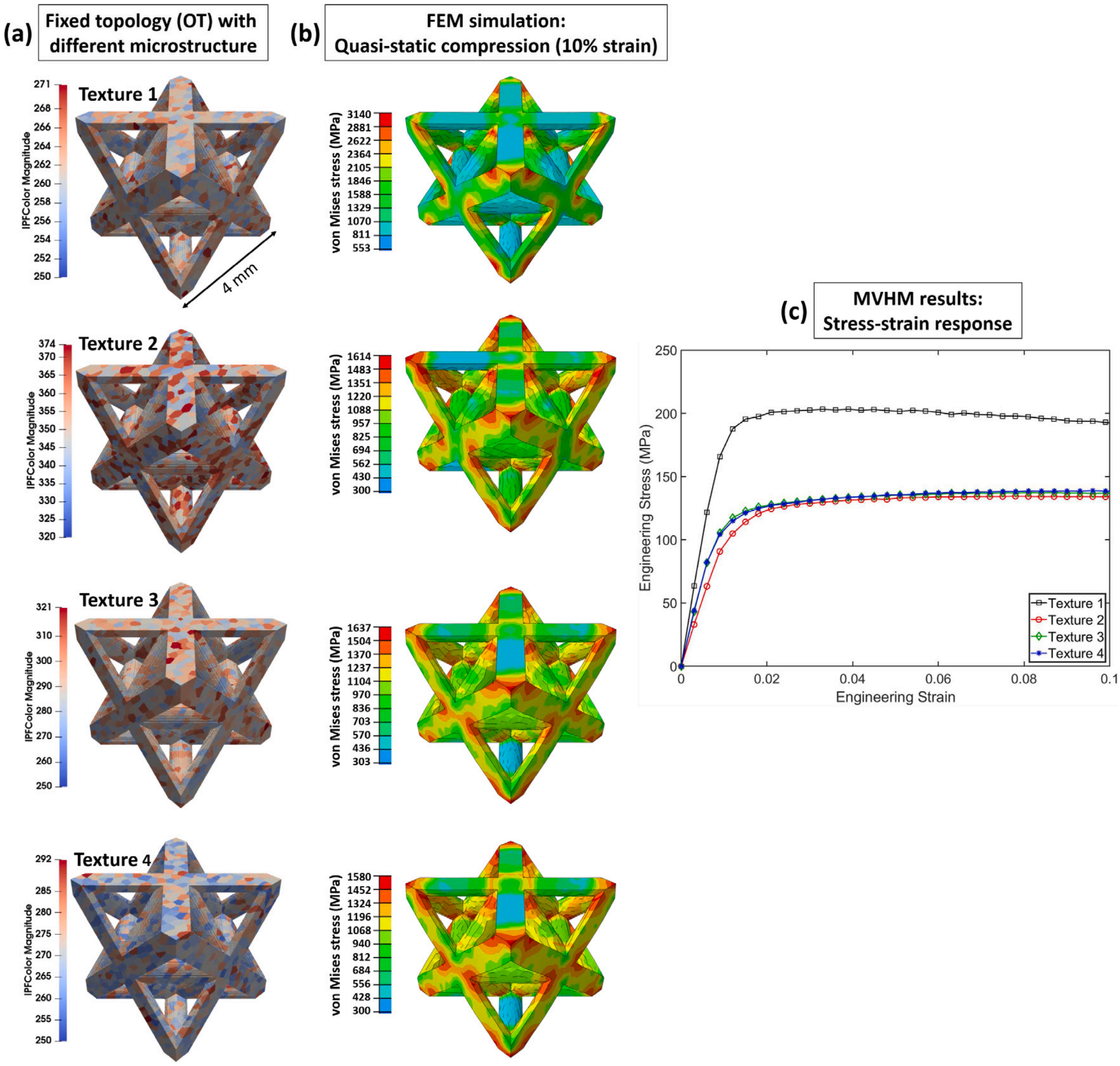

Fig. 13. The effect of different crystallographic orientation texture on the stress–strain response of a single unit cell Octet truss LS topology under uniaxial compression loading. (a) the OT topology is fixed while the microstructure is changing based on generated textures from Section 4.2, (b) von Mises stress distribution of OT topology from FEM simulation indicating the different response of individual textures to quasi-static compression loading, and (c) the predicted engineering stress–strain curve from the FEM simulation calculated using MVHM yield surface. As it can be noticed, T1 shows a superior yield strength and energy absorption capacity compared to the other texture.

active slip system is determined by the stress projection tensor P_{tot} (see Eqs. (5), (6), and (7)), and the initial active slip system is the one that first satisfies the following Eq. (15):

$$\mathbf{P}^{s}_{tot} : \boldsymbol{\sigma} = \tau_{cr} \tag{15}$$

For a given slip system s, the stress projection factor can be expressed as a function of the uniaxial loading direction, which can be defined with the unit vector v, as:

$$P^{s}_{tot} \equiv v \cdot \mathbf{P}^{s}_{tot} v \tag{16}$$

The stress projection factor Max (P^{s}_{tot}) is defined as the maximum values of P^{s}_{tot} over all slip system s. Eq. (16) indicates the dependency of the P^{s}_{tot} on loading direction. Therefore, by modifying the grain orientation the value of P^{s}_{tot} varies.

A single crystal orientation may be characterized with respect to a fixed reference frame by a set of Euler angles, which describe rotations from the sample coordinate frame to the crystal coordinate frame using the Bunge's convention of the Euler notation as $Q\left(\varphi_1, \phi, \varphi_2\right)$ [62]:

$$[Q] = \begin{bmatrix} c(\phi_2) & s(\phi_2) & 0 \\ -s(\phi_2) & c(\phi_2) & 0 \\ 0 & 0 & 1 \end{bmatrix} \begin{bmatrix} 1 & 0 & 0 \\ 0 & c(\varPhi) & s(\varPhi) \\ 0 & -s(\varPhi) & c(\varPhi) \end{bmatrix} \begin{bmatrix} c(\phi_1) & s(\phi_1) & 0 \\ -s(\phi_1) & c(\phi_1) & 0 \\ 0 & 0 & 1 \end{bmatrix} =$$

$$\begin{bmatrix} c(\phi_1)c(\phi_2) - s(\phi_1)s(\phi_2)c(\varPhi) & s(\phi_1)c(\phi_2) + c(\phi_1)s(\phi_2)c(\varPhi) & s(\phi_2)s(\varPhi) \\ -c(\phi_1)s(\phi_2) - s(\phi_1)c(\phi_2)c(\varPhi) & -s(\phi_1)s(\phi_2) + c(\phi_1)c(\phi_2)c(\varPhi) & c(\phi_2)s(\varPhi) \\ s(\phi_1)s(\varPhi) & -c(\phi_1)s(\varPhi) & c(\varPhi) \end{bmatrix} \tag{17}$$

where $c(\phi_1) = \cos(\phi_1), s(\phi_1) = \sin(\phi_1)$, etc.

Here we consider the strain-controlled boundary conditions corresponding to uniaxial tension and compression along the Z axis. Hence, in order to investigate the effect of the crystallographic orientation of the constituent single-crystal grains on the mechanical properties when the SVE is subjected to tensile and compressive loading, the component of transformation matrix $[Q]$ should be resolved along Z direction.

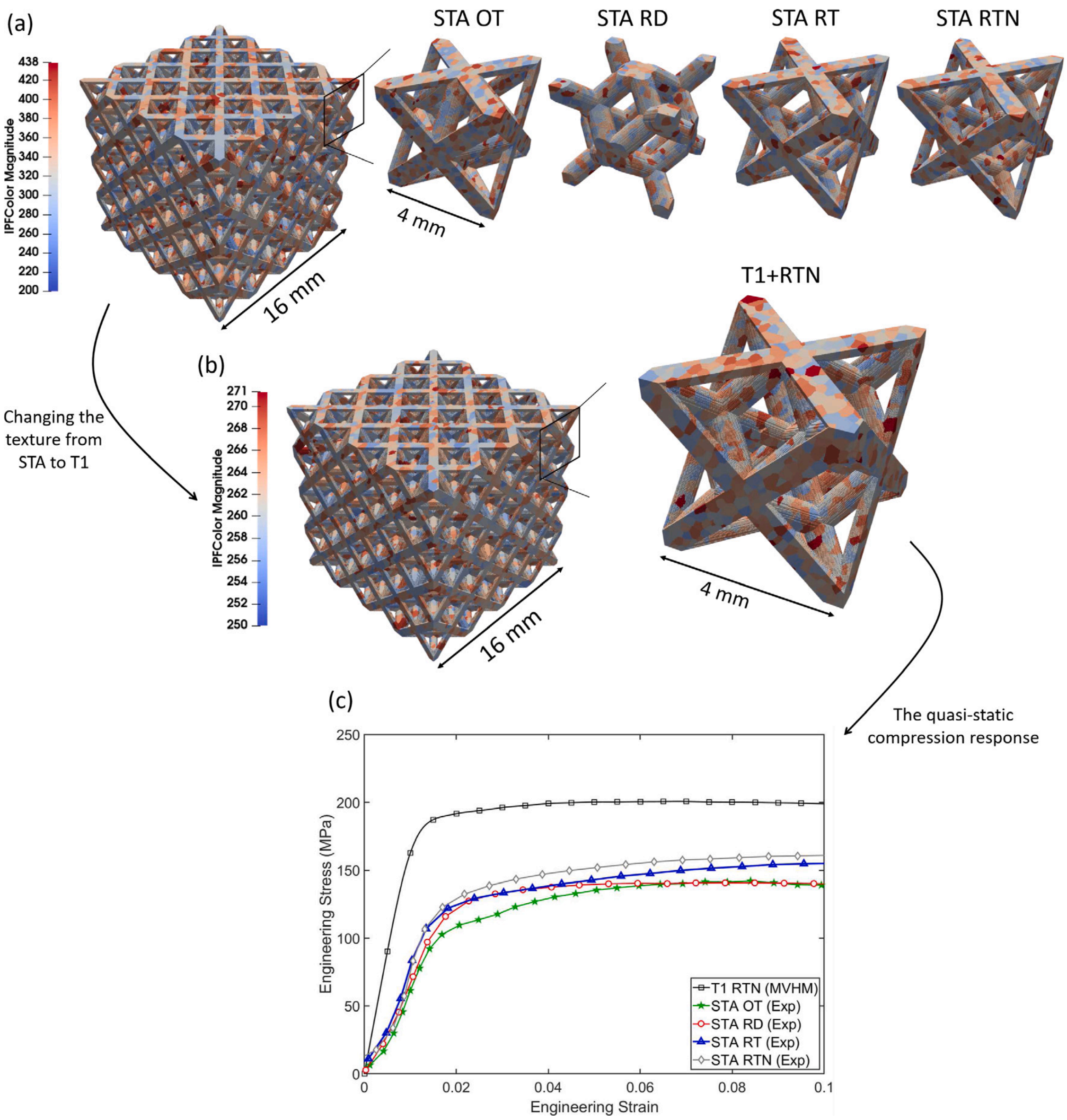

Fig. 14. The experimental results of quasi-static compression behavior of STA OT, RD, RT, and RTN topologies are compared with RTN topology with T1. (a) OT, RD, RT, and RTN topology with STA microstructure, (b) T1 is assigned to the RTN topology, which was created and optimized based on the deformation mechanisms of STA OT, RD, and RT topologies in our previous publication [1], (c) the mechanical behavior of RTN + T1 is compared to STA OT, RD, RT, and RTN topologies and the results show a significant improvement in yield strength, modulus of elasticity and energy absorption capacity.

Thus, $[\upsilon]$ in Eq. (16) is defined as follows:

$$[\upsilon] = [Q]\begin{bmatrix}0\\0\\1\end{bmatrix}_{Z_{axis}} = \begin{bmatrix}s(\phi_2)s(\Phi)\\c(\phi_2)s(\Phi)\\c(\Phi)\end{bmatrix} \tag{18}$$

Eq. (18) illustrates that only ϕ_2 and Φ affect the P^s_{tot} under uniaxial tension and compression loading along Z direction. Fig. 9 shows the effect of the crystallographic orientation of the constituent single-crystal grains i.e., ϕ_2 and Φ on the stress projection factor P^s_{tot}. Assuming that τ_{cr} is constant for all slip systems, the stress required to initiate slip under the applied stress, $\boldsymbol{\sigma}$, can be calculated from:

$$\tau_{cr} = \mathbf{P}^{\alpha}_{tot} : \boldsymbol{\sigma} \tag{19}$$

Thus, the yield stresses in uniaxial tension and compression are calculated as:

$$\sigma_{yt} = \frac{\tau_{cr}}{P^{T}_{tot}} \tag{20}$$

$$\sigma_{yc} = -\frac{\tau_{cr}}{P^{C}_{tot}} \tag{21}$$

where σ_{yt} and σ_{yc} are yield strength under uniaxial tension and compression, respectively. As it can be observed from Fig. 9, $P^s_{tot} = 0.54$ is maximum for tension at $\Phi = 24°$ and $\phi_2 = 25°$, while $P^s_{tot} = 0.48$ at $\Phi = 26°$ and $\phi_2 = 1°$ is maximum for uniaxial compression loading. From Eqs. (20) and (20), when P^{α}_{tot} is maximum, the yield strength is minimum and slip initiates easier. The minimum P^s_{tot} is 0.34 and 0.22 at $\Phi = 55°$ and $\phi_2 = 45°$ for both uniaxial tension and compression, respectively. Both tension and compression loading at $\Phi = 48°$ and $\phi_2 = 84°$ give the P^s_{tot} value of ≈ 0.45 and yielding is symmetric between tension and compression. In order to achieve higher tensile strength, $P^{C}_{tot} - P^{T}_{tot} > 0$ should be maximum. Therefore, the following orientation cases, listed in Table 3, were selected to generate technical single crystal with strong textures along those directions to analyze the effect of each texture on the mechanical behavior of IN718. In this study, the term technical single crystal refers to grain boundaries

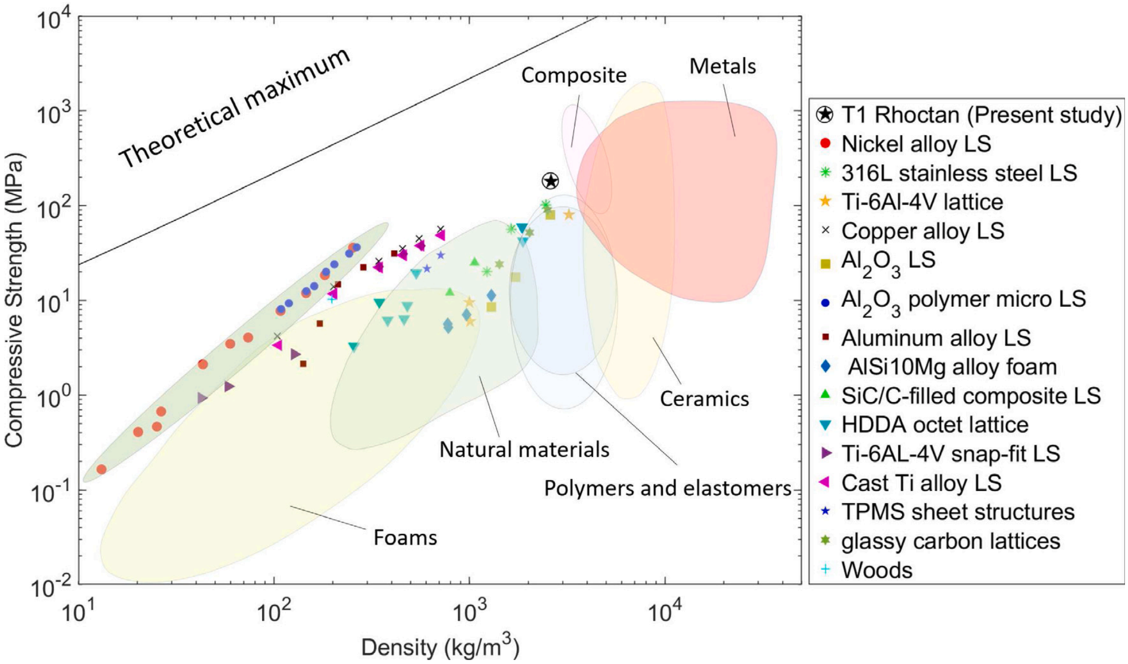

Fig. 15. Material property chart demonstrating the relationship between compressive strength of different metallic and non-metallic engineering material and density. The figure illustrates how the developed T1 RTN fill a new niche in the high-strength lightweight material parameter space. The theoretical maximum areas define regions that cannot be achieved under ambient conditions [1,22–24,24–34].

Table 3
Four different crystallographic texture orientation of the constituent single-crystal grains were chosen in order to investigate the effect of each case on the mechanical behavior of IN718.

Texture No.	P^s_{tot}	Φ	ϕ_2
Texture 1 (T1)	Min (P^s_{tot})	55°	45°
Texture 2 (T2)	Max (P^s_{tot})	24°	25°
Texture 3 (T3)	$P^T_{tot} = P^C_{tot}$	48°	84°
Texture 4 (T4)	Max ($P^C_{tot} - P^T_{tot} > 0$)	45°	90°

with a misorientation angle of up to 12° that are present inside the crystal [18]. The pole figures of the generated crystallographic texture orientation cases defined in Table 3, are illustrated in Fig. 10.

5. Results and discussion

As discussed in Section 3, three loading paths including tension, compression, and shear were simulated. These loading paths are used to characterize four different microstructures denoted by T1, T2, T3, and T4 (see Section 4.2). The generataed microstructures were used to fit the MVHM yield surface function. The quantitative predictions based on CP simulation results, such as global stress–strain response, are subject to variability. To quantify the variability of stress–strain response for different SVE realizations, three distinct microstructures with the same grain size distribution but different morphologies are created. Each microstructure is then examined, the results compared to experimental data. It should be pointed out that the mechanical response of all three generated microstructures were almost identical, implying there was no uncertainty in the final results.

The results of these simulations are then used to identify the parameters for the MVHM yield surface. After each simulation, the stress tensor for each loading case at a plastic work per unit volume (see Eq. (22)) of 2 MPa is determined and is used as a yield stress point. This value is chosen based on the experimental stress–strain response in which the yield point in 2 MPa plastic work per unit volume is equivalent to 0.2% offset yield strength. The plastic work per unit volume is calculated as the area under effective stress σ_{eff} and effective plastic strain ϵ^p_{eff} curve as defined in the following equation:

$$W_p = \int \sigma_{eff} d\epsilon^p_{eff} \tag{22}$$

The EVP-FFT simulation was performed in 40 increments of 0.05%, up to 2% percent strain for the tension and shear, and 100 increments of 0.1%, up to 10% percent strain for the uniaxial compression loading. Fig. 11 shows the EVP-FFT model predicted macroscopic stress–strain curve, including uniaxial tension, compression, and shear for all considered textures. According to Fig. 11a, Texture 1 with the minimum P^s_{tot} has the highest tensile and compressive yield strength, with a tensile yield strength of 1251 MPa and a compression yield strength of 1853 MPa. This represents a 20% and 58% yield strength improvement in tensile and compressive strength, respectively, compared to the original texture (i.e., experimental results of STA IN718). On the other hand, Texture 2 has the lowest yield strength, at 880 MPa for tension and 990 MPa for compression (see Fig. 11). As previously stated, IN718 demonstrates strength differential behavior, i.e., distinct plastic flow behaviors in tension and compression, with compressive yield strength being greater than tensile strength [16,17,49,50]. However, Fig. 11c and d indicate that by altering the crystallographic texture, this behavior may be controlled or even completely reversed. Texture 3 produces similar yield strength value under tension and compression (Fig. 11c), while the tensile yield strength of Texture 4 is around 10% greater than the compressive counterpart.

Finally, using the computed yield points obtained from the EVP-FFT simulations, which include tensile, compressive, and shear strength, the RMSD method is used to get the yield function (MVHM) parameters for each texture (see Section 3.1). As shown in Fig. 12, four distinct yield surfaces are generated for each of the textures. The initial yield surfaces from Fig. 12 then are used to analyze the mechanical behavior of different LS topologies under quasi-static compression loading using finite element method (Abaqus/Explicit). Meshes constructed of 4-node linear tetrahedral elements were used in the models (C3D4). Following that, the LSs were compressed between rigid plates assuming a coefficient of friction between the LS and the platens equal to 0.2. A general contact algorithm was defined and applied to the entire model

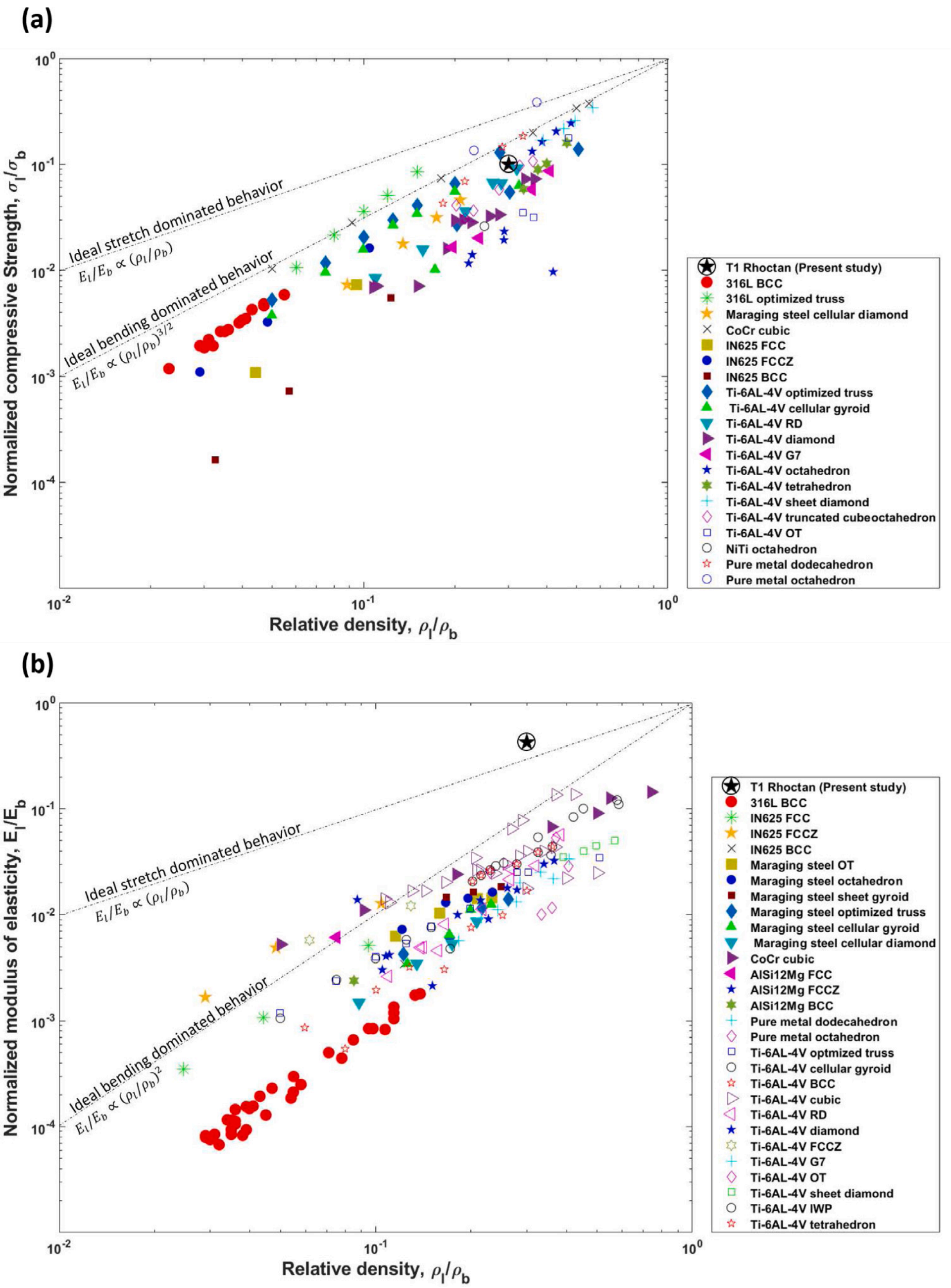

Fig. 16. Comparing the normalized (a) quasi static compressive strength, and (b) modulus of elasticity of RTN topology with texture 1 as a function of relative density with other metallic AMLS [35].

to account for the possibility of contact between struts during the deformation. More detailed information regarding the MVHM calibration, validation, and FEM setup and analysis of LS are provided in our recent publications [1,16].

Fig. 13 shows the effect of different crystallographic textures on the mechanical response of a unit cell with Octet truss (OT) topology under uniaxial compression loading. On average, T1 has 61% and 68% higher modulus of elasticity and yield strength than T2, T3, and T4, respectively. This clearly demonstrates how the mechanical response is influenced by the microstructure.

Previously, we developed a topology-microstructure-based optimization technique to investigate the interplay between the topology and microstructure by analyzing the deformation mechanisms of different LS topologies made of STA IN718 [1]. Using this approach, a new optimized topology named as Rhoctan (RTN) was created and validated experimentally. The generation process, geometrical details, and performance of the newly introduced RTN topology used in uniform and hybrid lattice structures are described in [1,63]. RTN demonstrated 53%, 25%, and 15% higher energy absorption capacity over the Octet Truss (OT), Rhombic Dodecahedron (RD), and Rhoctet (RT) topologies, respectively (see Fig. 14). Therefore, the crystallographic orientation T1, which possesses enhanced yield strength, modulus of elasticity, and energy absorption capacity (see Fig. 11), used in conjunction with the new topology optimized LS (RTN) further improves the mechanical performance relative to the IN718 STA microstructure. Fig. 14 compares the topology and quasi-static compression behavior of OT, RD, and RT with the newly developed topology RTN along with the T1 texture. The results from Fig. 14 demonstrate 50% improvement in both the yield strength and modulus of elasticity. This example shows that the design optimization method presented herein that accounts for the synergistic relationship between microstructure and topology enables researchers to explore the optimized balance between both variables for particular loading conditions.

To compare the yield strength of the new optimized topology-microstructure T1 RTN with other metallic and non-metallic engineering material and structures, an Ashby material property chart plotting the compressive yield strength versus the density is generated and presented in Fig. 15. As shown in Fig. 15, the yield strength of RTN topology containing T1 texture is comparable with composite structure and in comparison to Ti-6Al-4V LS provides higher strength at a lower density. The yield strenght of RTN topology with T1 texture is approximately two times greater than the yield strength of AMLS 316L stainless steel and Al_2O_3 with the same relative density, which marks a new entry into the high-strength lightweight material parameter space.

Fig. 16, also compares the normalized compressive strength and normalized modulus of elasticity of T1 RTN with other metallic AMLS data available in the pertinent literature [35]. The compressive strength (σ_l) and modulus of elasticity (E_l) of the LS are normalized by the compressive strength and Young's modulus of the building material (σ_b and E_b), respectively. The results indicate that the T1 RTN has considerably higher modulus of elasticity compared to other metallic AMLS and the yield strength is comparable to the other optimized LS with the same range of relative density.

From a manufacturing perspective, it has been shown that it is possible to control microstructure during the AM build process such as Electron Beam Powder Bed Fusion (EB-PBF) technique [18,19,64]. This may be accomplished by changing the process parameters and, in turn, carefully customizing the grain structure. With AM, it is now feasible to control the microstructural formation of the manufactured components as they are built. The presented work demonstrates a methodology for simultaneously optimizing grain size and texture for a given topology to meet specific design requirements and/or maximize LS mechanical properties.

6. Summary

In this study, we demonstrated a design methodology by integrating experiment, microscale modeling (material scale), and macroscale finite element modeling to determine an optimized combination of microstructure and topology that leads to improved mechanical properties of additively manufactured lattice structures (AMLS). The optimum microstructure is determined by using full-field polycrystal plasticity simulations to compute the effective macroscale material response by considering crystallographic texture to be the dominant design variable. Four different textures were considered based on stress projection factor analysis. The results from these simulations were used to parameterize a macroscale yield surface and hardening behavior for each of the considered textures. The microstructure-dependent macroscale model was then used in unit cell finite element simulations to predict the mechanical response of various lattice structure topologies.

The results show that in LS with fixed topology (OT), T1 in which $\langle 111 \rangle$ is parallel to the loading direction improved the compressive strength of the OT LS by approximately 68% compared to the other generated textures. However, when the T1 microstructure is combined with the RTN topology, the yield strength and modulus of elasticity are increased by 50% above previously optimized topologies that were considered using fixed microstructure. Therefore, the synergistic relationship between microstructure and topology can be made by leveraging the microstructure that works the best with the given topology. In other words, improved and/or tailored mechanical performance can be achieved by varying microstructure and topology simultaneously. It is envisioned that this methodology can be formalized, generalized, and automated leading to unique and non-intuitive LS designs that consider the interplay between topology and microstructure on engineering scale performance. The ability to control the spatial variation of local microstructure attributes that is possible through AM processes moves this conceptual approach from a theoretical consideration to a realizable design strategy.

CRediT authorship contribution statement

Behzad Bahrami Babamiri: Modeling, Data analysis, data interoperation, and writing manuscript. **Jason R. Mayeur:** Modeling, data interpretation, and section writing. **Kavan Hazeli:** Academic support, design experiments, section writing, data interpretation, and editing.

Declaration of competing interest

The authors declare that they have no known competing financial interests or personal relationships that could have appeared to influence the work reported in this paper.

Acknowledgment

This investigation was supported by Mechanics of Materials and Structures (MOMS), USA program at the National Science Foundation (NSF), USA under the Award Number: 1943465.

References

[1] Behzad Bahrami Babamiri, Baxter Barnes, Arash Soltani-Tehrani, Nima Shamsaei, Kavan Hazeli, Designing additively manufactured lattice structures based on deformation mechanisms, Addit. Manuf. 46 (2021) 102143.
[2] Yafeng Han, Wen Feng Lu, A novel design method for nonuniform lattice structures based on topology optimization, J. Mech. Des. 140 (9) (2018) 091403.
[3] Lorenzo Valdevit, A. Pantano, Howard A. Stone, Anthony G. Evans, Optimal active cooling performance of metallic sandwich panels with prismatic cores, Int. J. Heat Mass Transfer 49 (21–22) (2006) 3819–3830.
[4] Menghui Xu, Zhiping Qiu, Free vibration analysis and optimization of composite lattice truss core sandwich beams with interval parameters, Compos. Struct. 106 (2013) 85–95.
[5] Lin Cheng, Xuan Liang, Eric Belski, Xue Wang, Jennifer M. Sietins, Steve Ludwick, Albert To, Natural frequency optimization of variable-density additive manufactured lattice structure: theory and experimental validation, J. Manuf. Sci. Eng. 140 (10) (2018).
[6] Aamer Nazir, Kalayu Mekonen Abate, Ajeet Kumar, Jeng-Ywan Jeng, A state-of-the-art review on types, design, optimization, and additive manufacturing of cellular structures, Int. J. Adv. Manuf. Technol. 104 (9) (2019) 3489–3510.
[7] Yafeng Han, Wenfeng Lu, Evolutionary design of nonuniform cellular structures with optimized Poisson's ratio distribution, Mater. Des. 141 (2018) 384–394.
[8] Yafeng Han, Wen F. Lu, Optimization design of nonuniform cellular structures for additive manufacturing, in: International Manufacturing Science and Engineering Conference, Vol. 51357, American Society of Mechanical Engineers, 2018, V001T01A033.
[9] Stephen Daynes, Stefanie Feih, Wen Feng Lu, Jun Wei, Optimisation of functionally graded lattice structures using isostatic lines, Mater. Des. 127 (2017) 215–223.
[10] Mark C. Messner, Optimal lattice-structured materials, J. Mech. Phys. Solids 96 (2016) 162–183.
[11] Akihiro Takezawa, Yuichiro Koizumi, Makoto Kobashi, High-stiffness and strength porous maraging steel via topology optimization and selective laser melting, Addit. Manuf. 18 (2017) 194–202.
[12] G. Totaro, Z. Gürdal, Optimal design of composite lattice shell structures for aerospace applications, Aerosp. Sci. Technol. 13 (4–5) (2009) 157–164.
[13] Ji-Hong Zhu, Wei-Hong Zhang, Liang Xia, Topology optimization in aircraft and aerospace structures design, Arch. Comput. Methods Eng. 23 (4) (2016) 595–622.
[14] Fei Liu, David Z. Zhang, Peng Zhang, Miao Zhao, Salman Jafar, Mechanical properties of optimized diamond lattice structure for bone scaffolds fabricated via selective laser melting, Materials 11 (3) (2018) 374.
[15] Jun Wu, Niels Aage, Rüdiger Westermann, Ole Sigmund, Infill optimization for additive manufacturing—approaching bone-like porous structures, IEEE Trans. Vis. Comput. Graphics 24 (2) (2017) 1127–1140.
[16] Behzad Bahrami Babamiri, Hesam Askari, Kavan Hazeli, Deformation mechanisms and post-yielding behavior of additively manufactured lattice structures, Mater. Des. 188 (2020) 108443.
[17] Behzad Bahrami Babamiri, Joseph Indeck, Gabriel Demeneghi, Jefferson Cuadra, Kavan Hazeli, Quantification of porosity and microstructure and their effect on quasi-static and dynamic behavior of additively manufactured Inconel 718, Addit. Manuf. 34 (2020) 101380.

[18] Martin R. Gotterbarm, Mohsen Seifi, Daniel Melzer, Jan Džugan, Ayman A. Salem, Zhong H. Liu, Carolin Koerner, Small scale testing of IN718 single crystals manufactured by EB-PBF, Addit. Manuf. 36 (2020) 101449.

[19] A. Plotkowski, J. Ferguson, B. Stump, W. Halsey, V. Paquit, C. Joslin, S.S. Babu, A. Marquez-Rossy, M.M. Kirka, R.R. Dehoff, A stochastic scan strategy for grain structure control in complex geometries using electron beam powder bed fusion, Addit. Manuf. (2021) 102092.

[20] Ricardo A. Lebensohn, Anand K. Kanjarla, Philip Eisenlohr, An elasto-viscoplastic formulation based on fast Fourier transforms for the prediction of micromechanical fields in polycrystalline materials, Int. J. Plast. 32 (2012) 59–69.

[21] Devraj Ranjan, Sankar Narayanan, Kai Kadau, Anirban Patra, Crystal plasticity modeling of non-schmid yield behavior: from Ni3Al single crystals to Ni-based superalloys, Modelling Simul. Mater. Sci. Eng. 29 (5) (2021) 055005.

[22] Kavan Hazeli, Behzad Bahrami Babamiri, Joseph Indeck, Andrew Minor, Hesam Askari, Microstructure-topology relationship effects on the quasi-static and dynamic behavior of additively manufactured lattice structures, Mater. Des. 176 (2019) 107826.

[23] Tianlin Zhong, Ketai He, Huaixue Li, Lechang Yang, Mechanical properties of lightweight 316 L stainless steel lattice structures fabricated by selective laser melting, Mater. Des. 181 (2019) 108076.

[24] Liang Dong, Vikram Deshpande, Haydn Wadley, Mechanical response of Ti–6Al–4V octet-truss lattice structures, Int. J. Solids Struct. 60 (2015) 107–124.

[25] Lucas R. Meza, Satyajit Das, Julia R. Greer, Strong, lightweight, and recoverable three-dimensional ceramic nanolattices, Science 345 (6202) (2014) 1322–1326.

[26] Jens Bauer, Stefan Hengsbach, Iwiza Tesari, Ruth Schwaiger, Oliver Kraft, High-strength cellular ceramic composites with 3D microarchitecture, Proc. Natl. Acad. Sci. USA 111 (7) (2014) 2453–2458.

[27] Han Wang, Yu Fu, Mingming Su, Hai Hao, Effect of structure design on compressive properties and energy absorption behavior of ordered porous aluminum prepared by rapid casting, Mater. Des. 167 (2019) 107631.

[28] Lenko Stanev, Boris Drenchev, Anton Yotov, Rumiana Lazarova, Compressive properties and energy absorption behaviour of alsi10mg open-cell foam, J. Mater. Sci. Technol. 22 (1) (2014) 44–53.

[29] Brett G. Compton, Jennifer A. Lewis, 3D-printing of lightweight cellular composites, Adv. Mater. 26 (34) (2014) 5930–5935.

[30] Xiaoyu Zheng, Howon Lee, Todd H Weisgraber, Maxim Shusteff, Joshua DeOtte, Eric B. Duoss, Joshua D. Kuntz, Monika M. Biener, Qi Ge, Julie A. Jackson, et al., Ultralight, ultrastiff mechanical metamaterials, Science 344 (6190) (2014) 1373–1377.

[31] Qizhen Li, Edward Y. Chen, Douglas R. Bice, David C. Dunand, Mechanical properties of cast Ti-6Al-4V lattice block structures, Metall. Mater. Trans. A 39 (2) (2008) 441–449.

[32] Qizhen Li, Edward Y. Chen, Douglas R. Bice, David C. Dunand, Mechanical properties of cast Ti-6Al-2Sn-4Zr-2Mo lattice block structures, Adv. Energy Mater. 10 (10) (2008) 939–942.

[33] Lei Zhang, Stefanie Feih, Stephen Daynes, Shuai Chang, Michael Yu Wang, Jun Wei, Wen Feng Lu, Energy absorption characteristics of metallic triply periodic minimal surface sheet structures under compressive loading, Addit. Manuf. 23 (2018) 505–515.

[34] Alan J. Jacobsen, Sky Mahoney, William B. Carter, Steven Nutt, Vitreous carbon micro-lattice structures, Carbon 49 (3) (2011) 1025–1032.

[35] M. Benedetti, A. Du Plessis, R.O. Ritchie, M. Dallago, S.M.J. Razavi, F. Berto, Architected cellular materials: A review on their mechanical properties towards fatigue-tolerant design and fabrication, Mater. Sci. Eng.: R: Rep. 144 (2021) 100606.

[36] Michael A. Groeber, Michael A. Jackson, DREAM. 3D: a digital representation environment for the analysis of microstructure in 3D, Integr. Mater. Manuf. Innov. 3 (1) (2014) 56–72.

[37] Michael Anthony Groeber, Development of an Automated Characterization-Representation Framework for the Modeling of Polycrystalline Materials in 3D (Ph.D. thesis), The Ohio State University, 2007.

[38] Herve Moulinec, Pierre Suquet, A fast numerical method for computing the linear and nonlinear mechanical properties of composites, C. R. Acad. Sci. Ser. II Mec. Phys. Chimie Astron. (1994).

[39] Hervé Moulinec, Pierre Suquet, A numerical method for computing the overall response of nonlinear composites with complex microstructure, Comput. Methods Appl. Mech. Engrg. 157 (1–2) (1998) 69–94.

[40] Philip Eisenlohr, Martin Diehl, Ricardo A. Lebensohn, Franz Roters, A spectral method solution to crystal elasto-viscoplasticity at finite strains, Int. J. Plast. 46 (2013) 37–53.

[41] J.C. Michel, H. Moulinec, P. Suquet, A computational scheme for linear and non-linear composites with arbitrary phase contrast, Internat. J. Numer. Methods Engrg. 52 (1–2) (2001) 139–160.

[42] David J. Eyre, Graeme W. Milton, A fast numerical scheme for computing the response of composites using grid refinement, Eur. Phys. J. Appl. Phys. 6 (1) (1999) 41–47.

[43] Vincent Monchiet, Guy Bonnet, A polarization-based FFT iterative scheme for computing the effective properties of elastic composites with arbitrary contrast, Internat. J. Numer. Methods Engrg. 89 (11) (2012) 1419–1436.

[44] Ricardo A. Lebensohn, N-site modeling of a 3D viscoplastic polycrystal using fast Fourier transform, Acta Mater. 49 (14) (2001) 2723–2737.

[45] B. Liu, D. Raabe, F. Roters, P. Eisenlohr, R.A. Lebensohn, Comparison of finite element and fast Fourier transform crystal plasticity solvers for texture prediction, Modelling Simul. Mater. Sci. Eng. 18 (8) (2010) 085005.

[46] A. Prakash, R.A. Lebensohn, Simulation of micromechanical behavior of polycrystals: finite elements versus fast Fourier transforms, Modelling Simul. Mater. Sci. Eng. 17 (6) (2009) 064010.

[47] R.A. Lebensohn, Y. Liu, P. Ponte Castaneda, On the accuracy of the self-consistent approximation for polycrystals: comparison with full-field numerical simulations, Acta Mater. 52 (18) (2004) 5347–5361.

[48] Pratheek Shanthraj, Philip Eisenlohr, Martin Diehl, Franz Roters, Numerically robust spectral methods for crystal plasticity simulations of heterogeneous materials, Int. J. Plast. 66 (2015) 31–45.

[49] Saiganesh K. Iyer, Cliff J. Lissenden, Inelastic anisotropy of Inconel 718: experiments and mathematical representation, J. Eng. Mater. Technol. 122 (3) (2000) 321–326.

[50] Saiganesh K. Iyer, Cliff J. Lissenden, Multiaxial constitutive model accounting for the strength-differential in Inconel 718, Int. J. Plast. 19 (12) (2003) 2055–2081.

[51] Daniel J. Savage, Irene J. Beyerlein, Marko Knezevic, Coupled texture and non-schmid effects on yield surfaces of body-centered cubic polycrystals predicted by a crystal plasticity finite element approach, Int. J. Solids Struct. 109 (2017) 22–32.

[52] Miroslav Zecevic, Marko Knezevic, A new visco-plastic self-consistent formulation implicit in dislocation-based hardening within implicit finite elements: Application to high strain rate and impact deformation of tantalum, Comput. Methods Appl. Mech. Engrg. 341 (2018) 888–916.

[53] Paul A. Flinn, Theory of deformation in superlattices, Trans. Am. Inst. Min. Metall. Eng. 218 (1) (1960) 145–154.

[54] M. Yamaguchi, V. Paidar, D.P. Pope, V. Vitek, Dissociation and core structure of <110> screw dislocations in L12 ordered alloys I. Core structure in an unstressed crystal, Phil. Mag. A 45 (5) (1982) 867–882.

[55] J.S. Koehler, F. Seitz, Proposed experiments for further study of the mechanism of plastic deformation, J. Appl. Mech. (1947).

[56] D.M. Collins, H.J. Stone, A modelling approach to yield strength optimisation in a nickel-base superalloy, Int. J. Plast. 54 (2014) 96–112.

[57] P.H. Thornton, R.G. Davies, T.L. Johnston, The temperature dependence of the flow stress of the γ' phase based upon Ni 3 Al, Metall. Trans. 1 (1) (1970) 207–218.

[58] C. Tome, G.R. Canova, U.F. Kocks, N. Christodoulou, J.J. Jonas, The relation between macroscopic and microscopic strain hardening in FCC polycrystals, Acta Metall. 32 (10) (1984) 1637–1653.

[59] Franz Roters, Philip Eisenlohr, Luc Hantcherli, Denny Dharmawan Tjahjanto, Thomas R. Bieler, Dierk Raabe, Overview of constitutive laws, kinematics, homogenization and multiscale methods in crystal plasticity finite-element modeling: Theory, experiments, applications, Acta Mater. 58 (4) (2010) 1152–1211.

[60] V.D. Fachinotti, A.A. Anca, A. Cardona, A method for the solution of certain problems in least squares, Int. J. Numer. Methods Biomed. Eng. 27 (4) (2011) 595–607.

[61] Donald W. Marquardt, An algorithm for least-squares estimation of nonlinear parameters, J. Soc. Ind. Appl. Math. 11 (2) (1963) 431–441.

[62] H.J. Bunge, C. Esling, Texture development by plastic deformation, Scr. Metall. 18 (3) (1984) 191–195.

[63] Baxter Barnes, Behzad Bahrami Babamiri, Gabriel Demeneghi, Arash Soltani-Tehrani, Nima Shamsaei, Kavan Hazeli, Quasi-static and dynamic behavior of additively manufactured lattice structures with hybrid topologies, Addit. Manuf. 48 (2021) 102466.

[64] Michael M. Kirka, Yousub Lee, Duncan A. Greeley, Alfred Okello, Michael J. Goin, Michael T. Pearce, Ryan R. Dehoff, Strategy for texture management in metals additive manufacturing, Jom 69 (3) (2017) 523–531.